Extrusion-based additive manufacturing of Mg-Zn alloy scaffolds

Dong, J.; Tümer, N.; Leeflang, M. A.; Taheri, P.; Fratila-Apachitei, L. E.; Mol, J. M.C.; Zadpoor, A. A.; Zhou, J.

DOI
10.1016/j.jma.2021.11.018

Publication date
2022

Document Version
Final published version

Published in
Journal of Magnesium and Alloys

Citation (APA)
Dong, J., Tümer, N., Leeflang, M. A., Taheri, P., Fratila-Apachitei, L. E., Mol, J. M. C., Zadpoor, A. A., & Zhou, J. (2022). Extrusion-based additive manufacturing of Mg-Zn alloy scaffolds. *Journal of Magnesium and Alloys*, *10*(9), 2491-2509. https://doi.org/10.1016/j.jma.2021.11.018

Available online at www.sciencedirect.com

ScienceDirect

Journal of Magnesium and Alloys 10 (2022) 2491–2509

www.elsevier.com/locate/jma

Full Length Article

Extrusion-based additive manufacturing of Mg-Zn alloy scaffolds

J. Dong[a,*], N. Tümer[a], M.A. Leeflang[a], P. Taheri[b], L.E. Fratila-Apachitei[a], J.M.C. Mol[b], A.A. Zadpoor[a], J. Zhou[a]

[a] *Department of Biomechanical Engineering, Delft University of Technology, Delft 2628 CD, the Netherlands*
[b] *Department of Materials Science and Engineering, Delft University of Technology, Delft 2628 CD, the Netherlands*

Received 24 September 2021; received in revised form 26 October 2021; accepted 19 November 2021
Available online 11 December 2021

Abstract

Porous biodegradable Mg and its alloys are considered to have a great potential to serve as ideal bone substitutes. The recent progress in additive manufacturing (AM) has prompted its application to fabricate Mg scaffolds with geometrically ordered porous structures. Extrusion-based AM, followed by debinding and sintering, has been recently demonstrated as a powerful approach to fabricating such Mg scaffolds, which can avoid some crucial problems encountered when applying powder bed fusion AM techniques. However, such pure Mg scaffolds exhibit a too high rate of *in vitro* biodegradation. In the present research, alloying through a pre-alloyed Mg-Zn powder was ultilized to enhance the corrosion resistance and mechanical properties of AM geometrically ordered Mg-Zn scaffolds simultaneously. The *in vitro* biodegradation behavior, mechanical properties, and electrochemical response of the fabricated Mg-Zn scaffolds were evaluated. Moreover, the response of preosteoblasts to these scaffolds was systematically evaluated and compared with their response to pure Mg scaffolds. The Mg-Zn scaffolds with a porosity of 50.3% and strut density of 93.1% were composed of the Mg matrix and $MgZn_2$ second phase particles. The *in vitro* biodegradation rate of the Mg-Zn scaffolds decreased by 81% at day 1, as compared to pure Mg scaffolds. Over 28 days of static immersion in modified simulated body fluid, the corrosion rate of the Mg-Zn scaffolds decreased from 2.3 ± 0.9 mm/y to 0.7 ± 0.1 mm/y. The yield strength and Young's modulus of the Mg-Zn scaffolds were about 3 times as high as those of pure Mg scaffolds and remained within the range of those of trabecular bone throughout the biodegradation tests. Indirect culture of MC3T3-E1 preosteoblasts in Mg-Zn extracts indicated favorable cytocompatibility. In direct cell culture, some cells could spread and form filopodia on the surface of the Mg-Zn scaffolds. Overall, this study demonstrates the great potential of the extrusion-based AM Mg-Zn scaffolds to be further developed as biodegradable bone-substituting biomaterials.

Keywords: Additive manufacturing; Material extrusion; Magnesium-zinc alloy; Porous scaffold; Biodegradation.

1. Introduction

Owing to their natural biodegradability, favorable mechanical properties, good biocompatibility, and osteopromotive activity [1–3], magnesium (Mg) and its alloys hold great promise for application as orthopedic implants. When developing a new generation of bone substitutes, the geometrical design of the implant should be also critically considered. Porous structures are generally preferred for bone regeneration, since a fully interconnected pore network with sufficient permeability and a large bio-functionalized surface area facilitates the proliferation and differentiation of cells [1–3]. The recent advent of additive manufacturing (AM) opens up new opportunities for the rational design of porous Mg to be developed as an ideal bone substitute, since AM can precisely control and fabricate geometrically complex parts with net or near-net shapes that are otherwise unattainable [4, 5].

Powder bed fusion AM techniques are the most commonly investigated AM technologies for the fabrication of porous metallic implants [1, 4, 6-9]. However, AM of porous Mg is

---

[*] Corresponding author: Delft University of Technology: Technische Universiteit Delft, the Netherlands
E-mail address: J.Dong-5@tudelft.nl (J. Dong).

https://doi.org/10.1016/j.jma.2021.11.018

still in its infancy with limited success [10–12], due to serious challenges and issues involved in the powder bed fusion-based AM of Mg. These challenges are often associated with the intrinsic properties of Mg, such as high vapor pressure and great affinity for oxygen, which lead to changes in the chemical composition and severe oxidation of the resulting materials [13, 14]. Given these limitations related to the AM processes with high energy power sources, employing an AM technique that operates at ambient temperature is more practical for fabricating Mg and its alloys.

Recently, (near) room temperature AM techniques, including powder bed solvent jetting [15, 16], fused filament fabrication [17], and ink extrusion-based AM [18] have been investigated for the fabrication of Mg-based materials. While the first two techniques have not been used for the fabrication of porous Mg structures, the ink extrusion-based AM technique has been successfully applied to fabricate Mg scaffolds with a fully interconnected structure [18]. Briefly, a two-step AM process has been developed, in which Mg green scaffolds printed at the first step are transformed into sintered Mg functional scaffolds through debinding and sintering at the second step [18]. These experiments have shown that room-temperature 3D printing processes can, indeed, avoid the challenges encountered in powder bed fusion AM of Mg scaffolds. The extrusion-based pure Mg scaffolds have been extensively studied in terms of their mechanical, biodegradation, and biological properties. It has been shown that pure Mg scaffolds with a highly interconnected pore structure degrade too fast, although their mechanical properties are acceptable. While surface modification can be used for improving the corrosion resistance of such materials, coatings can only provide effective protection at the beginning of biodegradation. After the coating is degraded or penetrated through, the exposed Mg substrate will dominate the overall biodegradation process [19]. To properly address this challenge, the corrosion resistance of the Mg substrate should be improved.

Alloying is one of the strategies that can effectively slow down the biodegradation of Mg by an order of magnitude or more [20]. Zinc (Zn) has been extensively studied as a common alloying element for Mg and has been shown to enhance both the corrosion resistance and mechanical properties of Mg [20–25]. According to the literature [26, 27], adding $<$ 6 wt% of Zn to Mg leads to a balanced combination of mechanical, corrosion, and biological properties, while 4 wt% of Zn results in an optimal grain refinement and improved mechanical properties. Moreover, unlike other frequently used alloying elements (*e.g.*, Al or rare earth elements), Zn is one of the most abundant, essential elements in the human body and plays an important role in bone formation, mineralization, and preservation [28]. Indeed, *in vivo* studies have confirmed that Mg-Zn binary alloys have a great potential to serve as orthopedic implants [23, 29, 30]. To date, porous Mg-Zn foams have been developed through the conventional powder metallurgy methods [21, 31, 32]. However, no reports on geometrically ordered porous Mg-Zn scaffolds have appeared in the literature.

In this study, a pre-alloyed Mg-Zn (4 wt% Zn) powder was chosen as the starting material and Mg-Zn binary alloy scaffolds with a geometrically ordered and fully interconnected porous structure were fabricated using extrusion-based AM. The biodegradation, mechanical, and biological behaviors of these scaffolds were then characterized. Pure Mg scaffolds fabricated using a similar approach served as a reference group to study the effects of Zn addition on the properties of the resulting biomaterials.

2. Materials and methods

2.1. Scaffold manufacturing

A cylindrical porous scaffold with a diameter of 12.38 mm and a height of 12.64 mm was designed (Fig. 1a). A lay-down pattern of 0°/90°/0° was adopted (Fig. 1b) for the scaffold and was designed using a custom software package associated with the 3D BioScaffolder printer (BS 3.2, GeSim, Germany). Pure Mg powder (impurity $<$0.01 wt%) and Mg-Zn powder (95.6 wt% Mg, 4.1 wt% Zn and 0.3 wt% impurities, Fig. 1c) with a spherical particle shape and median particle sizes of 44.96 μm and 37.7 μm, respectively, were used as the starting materials (Tangshan Weihao Magnesium Powder Co., China). The mean grain size of the Mg-Zn powder was 2.8 ± 0.1 μm (Fig. 1d) while that of the pure Mg powder was 8.6 ± 1.7 μm [19], which was determined by using the line intercept method after etching the powder particle cross-section in a solution composed of nitric acid, acetic acid, water, and ethanol at a volume ratio of 1:3:4:12.

Powder loaded inks were prepared by mixing the Mg powder with a binder system composed of hexane and polyisobutylene polymer ($M_w \sim 500{,}000$, Sigma Aldrich, Germany). The ink was loaded into a syringe (Nordson EFD, Germany) and was then extruded into 3D porous scaffolds through a 580 μm tapered nozzle tip using the 3D BioScaffolder printer. The deposition angles were of 0° and 90°, which were interchanged every layer. A printing pressure of 140–160 kPa and a speed of 5 mm/s were used for 3D printing. After 3D printing, the as-printed Mg-Zn and pure Mg scaffolds were loaded into a tube furnace (STF16/180, Carbolite Gero Ltd., UK) under a controlled argon atmosphere (purity $\geq$ 99.9999%; inlet pressure: 1 bar) for debinding and sintering. The as-printed Mg-Zn scaffolds and pure Mg scaffolds were respectively heated to 580 °C and 640 °C at 5 °C/min with a dwelling time of 1 h, followed by furnace cooling. The as-sintered Mg-Zn and pure Mg scaffolds were ultrasonically cleaned in isopropyl alcohol for 10 min prior to the subsequent characterization steps.

2.2. Characterization of the fabricated scaffolds

The morphology of the as-printed Mg-Zn scaffolds as well as the morphologies and the cross-section microstructures of the as-sintered Mg-Zn and pure Mg scaffolds were examined using a scanning electron microscope (SEM, JSM-IT100,

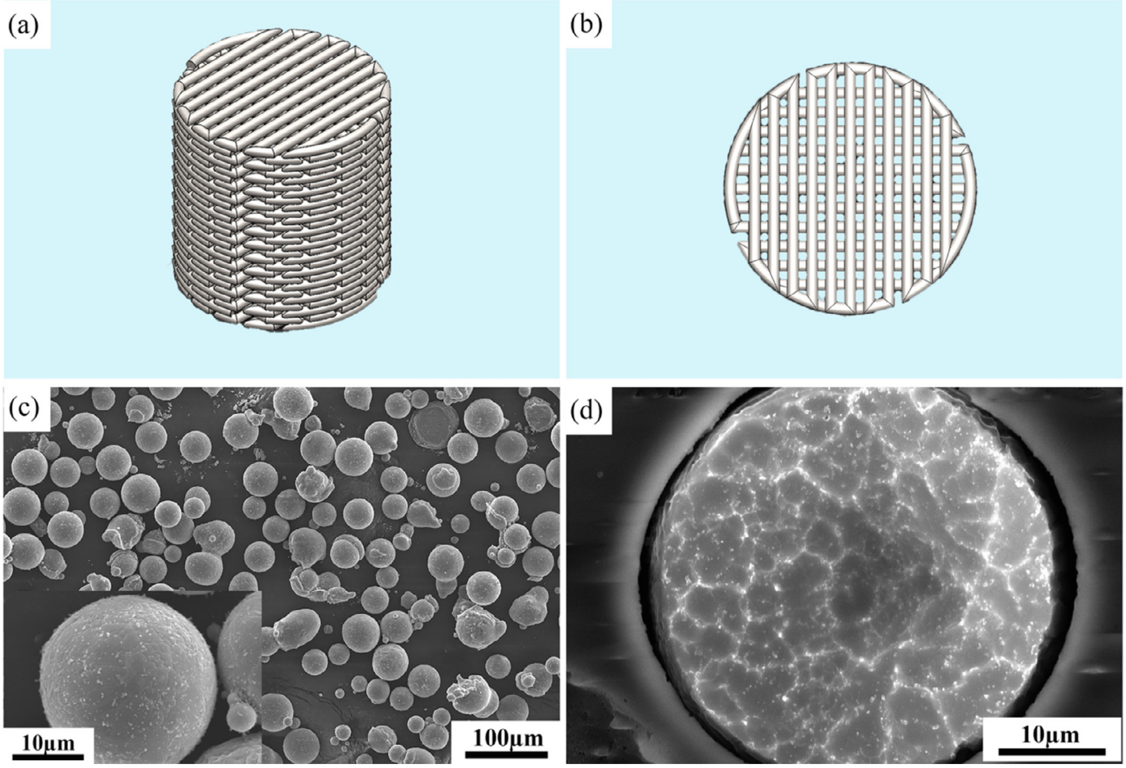

Fig. 1. The design of scaffolds and the Mg-Zn powder using for scaffold manufacturing: (a) CAD design, (b) lay-down pattern of the scaffold design, (c) pre-alloyed Mg-Zn powder particle morphology and (d) microstructure of the etched pre-alloyed Mg-Zn powder.

JEOL, Japan). The microporosity of the struts was measured from the SEM images taken on the polished cross sections using ImageJ (National Institutes of Health, USA). The polished Mg-Zn and pure Mg scaffold struts were etched using the same method as for the Mg-Zn powder. The etched specimens were then observed using the same SEM. The absolute porosities of the as-printed and as-sintered scaffolds were calculated using the following equations, based on the weighing method:

$$\varphi_p = \left(1 - \frac{\frac{m_p}{\rho_p}}{V_{bulk}}\right) \times 100\% \tag{1}$$

$$\varphi_s = \left(1 - \frac{\frac{m_s}{\rho_{Mg}}}{V_{bulk}}\right) \times 100\% \tag{2}$$

where φ_p and φ_s are, respectively, the absolute porosities of the as-printed and the as-sintered Mg-Zn and pure Mg scaffolds [%], m_p and m_s are, respectively, the masses of the as-printed and as-sintered Mg-Zn scaffolds or those of the pure Mg scaffold [g], V_{bulk} is the bulk volume of the scaffolds [cm^3], $\rho_p$is the density of the as-printed scaffolds, and ρ_{Mg} is the theoretical density of Mg (*i.e.*, 1.74 g/cm^3). The pore size distribution and the corresponding differential and cumulative intrusion volumes of the Mg-Zn and pure Mg scaffolds were measured using a mercury intrusion porosimeter (MIP, Micromeritics Autopore IV 9500) at pressures over the range of 0 to 210 MPa.

The phases present in the Mg-Zn scaffolds were identified using an X-ray diffractometer (XRD, Bruker D8 Advance diffractometer in Bragg-Brentano geometry). The X-ray diffractometer was equipped with a graphite monochromator and a Vantec position-sensitive detector that was set to work at 45 kV and 40 mA. A scan range of 20–100° and a step size of 0.030° using the Cu $K\alpha$ radiation were employed.

2.3. In vitro *immersion tests*

In vitro immersion tests of the Mg-Zn scaffolds were performed in revised simulated body fluid (r-SBF) [33] for up to 28 days in a thermal bath maintained at 37 °C. The same tests of the pure Mg scaffolds were performed only for 1 day. 450 mL of the r-SBF solution was used for the immersion tests of each specimen with a solution volume-to-surface area ratio of 7 mL/cm^2 (the surface area was calculated based on the CAD design) [34]. The changes of the pH values measured close to the outer surface of the specimens and further away from it were monitored using two pH micro electrodes (inlabNMR, METTLER TOLEDO). An inductively coupled plasma optical emission spectroscope (ICP-OES, iCAP 6500 Duo Thermo Fisher) was used to determine the concentrations of Mg, calcium (Ca), phosphate (PO_4^{3-}), and Zn ions in the r-SBF solution after the immersion tests of Mg-Zn and pure Mg scaffold samples at different time points.

X-ray micro-computed tomography (μCT, Nanotom 180 NF, GE Phoenix) scans of the Mg-Zn and pure Mg scaffolds before and after the immersion tests were acquired with a resolution of 6 μm. DICOM images of the scanned samples were imported into Dragonfly (Object Research Systems, Canada). After segmenting the corrosion products using Dragonfly, the volumes of the pure Mg and Mg-Zn specimens before and after the immersion tests were calculated by using the plugin "bone analysis". The volume loss was calculated according to the following equation:

$$Volume\ loss\ [\%] = \frac{\left(V_{Mg\ before\ degradation} - V_{Mg\ after\ degradation}\right)}{V_{Mg\ before\ degradation}} \times 100\% \qquad (3)$$

where $V_{\mathrm{Mg\ before\ degradation}}$ and $V_{\mathrm{Mg\ after\ degradation}}$ are the volumes of the specimens before and after the immersion test, respectively.

The average corrosion rates of Mg-Zn and pure Mg scaffolds were determined using the following equation according to ASTM G1–03:

$$Corrosion\ rate\ \left[mm/y\right] = 8.76 \times 10^4 \times \frac{V}{A \times t} \qquad (4)$$

where V is the loss of volume [g] (*i.e.*, $V_{Mgbeforedegradation}\ V_{Mgafterdegradation}$), A is the surface area of scaffold sample [cm^2], and t is the duration of *in vitro* immersion test [h].

In addition, the spacing between the struts of the Mg-Zn scaffolds that were retrieved after immersion for various durations (*i.e.*, 1, 3, 7, 14 and 28 days) was determined using the plugin "bone analysis" in Drangonfly. Furthermore, the volumes and porosities of the retrieved Mg-Zn scaffolds (including the corrosion products) were determined.

2.4. Characterization of in vitro corrosion products

Fourier-transform infrared spectroscopy (FTIR) spectra of the biodegraded Mg-Zn and pure Mg scaffolds were obtained by using a FTIR apparatus (Thermo-Nicolet Nexus, USA) equipped with a liquid-nitrogen cooled MCT-A (mercury-cadmium-telluride) detector and a SAGA grazing angle accessory at an incident angle of 80° with the setting of 128 scans at a resolution of 2 cm^{-1}. The Mg-Zn and pure Mg scaffolds before *in vitro* biodegradation were used for collecting the infrared background with the same settings. In addition, X-ray photoelectron spectroscopy (XPS, Thermo Fisher Scientific, K-Alpha Model, USA) was used to characterize the surface chemical states of the biodegraded Mg-Zn scaffolds after 1, 3, 7, 14, and 28 days of immersion. The measurements were performed under normal emission at a spot size of 400 μm and a base pressure of 10^{-7} mbar using a monochromatic Al Kα X-ray source. The Thermo Scientific Avantage v5.903 software (Thermo Fisher Scientific, USA) was used for processing and peak fitting. The surface morphologies and cross-section microstructures of the biodegraded Mg-Zn and pure Mg scaffolds at the selected time points were examined using the same SEM as before, equipped with an energy-dispersive X-ray spectroscope (EDS).

2.5. Electrochemical tests

The specimens (Mg-Zn or pure Mg) were connected to a copper wire using copper foil tape and were then mounted into epoxy resin. The surface area of the specimens exposed to the electrolyte was 12.37 cm^2. Electrochemical tests were performed in triplicate using a Bio-Logic SP-200 potentiostat (Bio-Logic Science Instruments, France) in the r-SBF solution at 37 °C. A three-electrode electrochemical cell was set up with graphite as the counter electrode, Ag/AgCl as the reference electrode, and Mg-Zn or pure Mg scaffold sample as the working electrode.

Potentiodynamic polarization (PDP) measurements were performed after stabilization of the open circuit potential (OCP) at 1 h of exposure. Then, the specimen was polarized from −0.3 V to +0.5 V versus OCP at a scan rate of 0.5 mV/s.

The Tafel extrapolation method was used for determining the corrosion potential E_{corr} and corrosion current density i_{corr}. The corrosion rates (CR) were calculated according to the obtained i_{corr}, based on the ASTM standard G102–89:

$$CR_{eletrochemical}\left[mm/y\right] = 3.27 \times 10^{-3} \times EW \times \frac{i_{corr}}{\rho} \qquad (5)$$

where EW is the equivalent weight of Mg (valence 2), i_{corr} is the current density [$\mu\mathrm{A/cm}^2$], and ρ is the theoretical density of Mg [$\mathrm{g/cm}^3$].

The linear polarization resistance (LPR) of the scaffold sample was measured consecutively at distinct exposure times up to 21 days at ± 25 mV versus OCP at a potential sweep rate of 0.167 mV s^{-1}.

2.6. Mechanical properties

Uniaxial compression tests of the as-fabricated Mg-Zn scaffold specimens as well as the Mg-Zn scaffold specimens retrieved after 1, 3, 7 and 14 days of *in vitro* immersion were performed using an Instron universal mechanical testing machine (ElectroPuls E10000, Germany) with a 10 kN load cell at a crosshead speed of 2 mm/min (initial strain rate: 0.003 s^{-1}). The mechanical properties of the scaffolds, including their elastic modulus and yield strength were obtained according to the ISO 13,314: 2011 standard. The slope of the initial linear region of the stress-strain curve was defined as the elastic modulus. An 0.2% strain offset line parallel to the initial linear elastic region was drawn and the stress value at the intersection with the stress-strain curve was defined as the yield stress.

2.7. Cytocompatibility evaluation

2.7.1. Preculture of cells and preparation of extracts

Preosteoblasts MC3T3-E1 (Sigma Aldrich, Germany) were pre-cultured for 7 days in α-minimum essential medium (α-MEM, Thermo Fisher Scientific, USA) without ascorbic acid, but supplemented with 10% fetal bovine serum (FBS, Thermo Fisher Scientific, USA) and 1% penicillin/streptomycin (p/s, Thermo Fisher Scientific, USA) under physiological conditions (5% CO_2 and 37 °C). The medium was refreshed once every 2–3 days.

The extracts of the Mg-Zn and pure Mg scaffolds were prepared by immersing the sterilized Mg-Zn and pure Mg scaffolds with a diameter of 10 mm and a height of 5 mm in α-MEM (without ascorbic acid but with 10% FBS and 1% p/s) under the abovementioned physiological conditions for 72 h The specimen-to-medium ratio was 1.25 cm^2/mL [35]. Afterwards, 100%, 50%, and 10% extracts of Mg-Zn and pure Mg were obtained by collecting, filtering, and diluting the corresponding supernatants. The pH values of these extracts were measured by using a pH meter (METTLER TOLEDO). The concentrations of the released Mg and Zn ions in those extracts were measured using ICP-OES (iCAP 6500 Duo Thermo Fisher, USA).

2.7.2. Indirect cytotoxicity tests

PrestoBlue assay (Thermo Fisher Scientific, USA) was used to evaluate the indirect cytocompatibility of the Mg-Zn and pure Mg scaffolds. First, 1×10^4 MC3T3-E1 preosteoblast cells were cultured in α-MEM (without ascorbic acid but with 10% FBS and 1% p/s) for 24 h, prior to exchanging the α-MEM with the 100%, 50%, and 10% Mg-Zn or pure Mg extracts ($n = 4$/group). The same number of cells was cultured in the original α-MEM (without ascorbic acid but with 10% FBS and 1% p/s) as the negative control. After 1, 3, and 7 days of culture, the Mg-Zn and pure Mg extract media were replaced with α-MEM (without ascorbic acid but with 10% FBS and 1% p/s) to prevent any interference between the extract and the tetrazolium salt [36], prior to adding the PrestoBlue reagent. Thereafter, the specimens were incubated with 50 μL of the PrestoBlue reagent at 37 °C for 1 h The absorbance values were then measured using a Victor X3 microplate reader (Perkin Elmer, The Netherlands) over a wavelength range of 530 - 590 nm. The average metabolic activity of the cells was calculated according to the following equation:

$$Metabolic\ activity\ [\%] = \frac{Absorbance\ (Mg\ specimen)}{Absorbance\ (negative\ control)} \times 100\% \quad (6)$$

Furthermore, rhodamine phalloidin and 4′,6-diamidino-2-phenylindole (DAPI) dyes were used to stain the cytoskeleton and nucleus of the cells in order to observe the morphology of the cells grown in the extracts. Therefore, MC3T3-E1 cells (number = 5×10^3) were cultured on 48-well glass disks in 200 μL extracts ($n = 2$). After 3 days of cell culture, the specimens were washed with phosphate buffered saline (PBS, Sigma-Aldrich, Germany) and were then fixed using 4% formaldehyde/PBS (Sigma-Aldrich, Germany) for 15 min at room temperature. Afterwards, the specimens were permeabilized with 0.5% Triton/PBS at 4 °C for 5 min. Then, 1% bovine serum albumin (BSA)/PBS (Sigma-Aldrich, Germany) was added per well, followed by incubation for 5 min. Consecutively, 1:1000 rhodamine phalloidin (Thermo Fisher Scientific, USA) in 1% BSA/PBS was added per well, followed by incubation for 1 h at 37 °C and three times wash with 0.5% Tween/PBS (Sigma-Aldrich, Germany). Then, the glass disks specimens were taken out of the wells and were mounted on glass slides with Prolong gold (containing 4′,6-diamidino-2-phenylindole (DAPI), Life Technologies, USA). A fluorescence microscope (ZOE fluorescent cell imager, Bio-Rad, USA) was then employed to observe the cytoskeleton and nuclei of the cells.

2.7.3. Direct cytotoxicity tests

To observe the distribution and morphology of the MC3T3-E1 cells seeded on the Mg-Zn scaffolds, a live/dead staining assay was performed. A total of 4×10^5 cells were seeded on the scaffolds (height = 2.4 mm, diameter = 9.3 mm, $n = 2$) in 48-well plates, which were then cultured in 1 mL of α-MEM (without ascorbic acid but with 10% FBS and 1% p/s). After 2.5 h (to allow for the attachment of the cells to the specimens), the scaffolds together with 1 mL α-MEM were transferred to 6-well plates. Additional α-MEM (7 mL) was added to the wells to reach a specimen-to-medium ratio of 1.25 cm^2/mL. After 3 days of cell culture, the specimens were taken out of the cultured medium and the medium was stored. Afterwards, the specimens were washed with PBS and were incubated in a PBS solution containing 0.5 μL/mL of calcein and 1.5 μL/mL of ethidium homodimer-1 (LIVE/DEAD Viability/Cytotoxicity Kit, Life Technologies Corp., USA) for 15 min in the dark at room temperature. The PBS solution was then replaced by the previously stored medium to prevent further reaction between the PBS solution and Mg-Zn scaffolds during the imaging process. Thereafter, the live and dead cells on the scaffolds were observed with a fluorescence microscope (ZOE cell imager, Bio-Rad, USA). Furthermore, the morphology of cells on the Mg-Zn scaffolds was observed under the same SEM. After 3 days of cell culture, the specimens ($n = 2$) were washed with PBS and were fixed with 4% formaldehyde (Sigma Aldrich, Germany) for 15 min, followed by dehydration stages in 50, 70, and 100% ethanol for 10 min each. They were further preserved by immersion in hexamethyldisilazane (Sigma Aldrich, Germany) for 30 min. The specimens were then dried overnight prior to SEM imaging.

2.8. Statistical analysis

Statistical analyses of the concentrations of Mg ion release and the metabolic activity results obtained from the indirect cytotoxicity tests were performed with ANOVA, followed by the Tukey *post hoc* test ($\alpha = 0.05$) with $p < .0001$, ****; $p < .001$, ***; $p < .01$ and **; $p < .05$, *.

3. Results

3.1. Structural characteristic of the scaffolds

The as-printed Mg-Zn and pure Mg scaffolds with freestanding characteristics were similar in their exterior

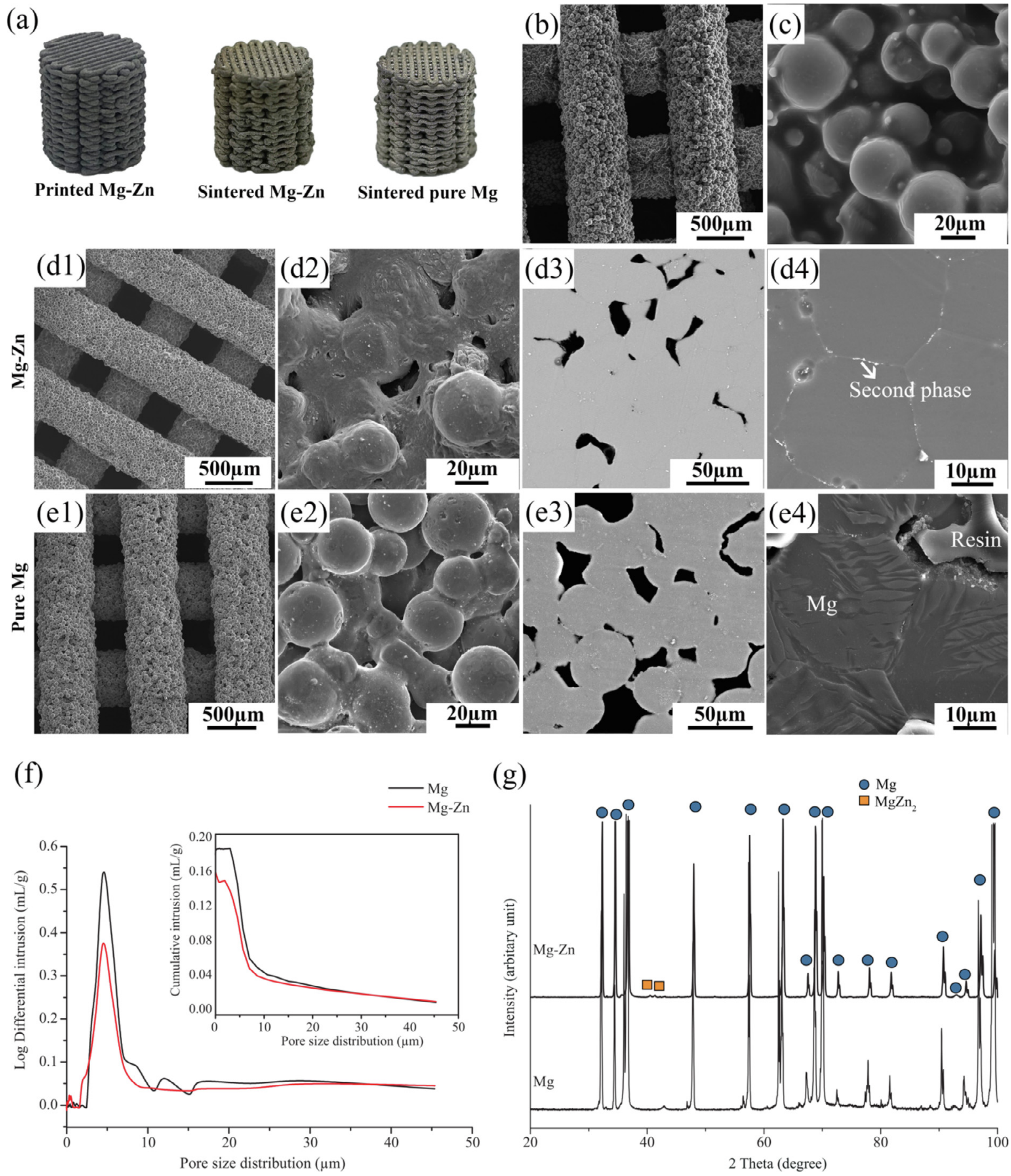

Fig. 2. Characteristics of the fabricated Mg-Zn scaffolds in comparison with those of the pure Mg scaffolds: (a) macrographs, (b and c) the morphologies of the as-printed Mg-Zn scaffold struts at different magnifications, (d1-d4) the morphology, cross-section and microstructure of the as-sintered Mg-Zn scaffolds, (e1-e4) the morphology, cross-section and microstructure of the as-sintered pure Mg scaffolds, (f) micropore size distributions in the struts (the plot of pure Mg cited from [18]), and (g) XRD patterns (the pattern of pure Mg cited from [18]).

appearance to the design. After sintering, the dimensions of the Mg-Zn and pure Mg scaffolds were reduced by 10.7 ± 0.1% and 9.5 ± 0.2%, respectively (Fig. 2a). The struts of the top layer of the printed Mg-Zn scaffolds perpendicularly bridged the struts of the underlying layer, precisely as designed (Fig. 2b). The powder particles were evenly embedded in the binder (Fig. 2c). Sufficient powder loading in the ink allowed the scaffolds with a high aspect ratio to be built with almost no distortions. The as-printed Mg-Zn and pure Mg scaffolds had similar micro-porosities, and the strut width and spacing values were quite close to the design values (Table 1). After sintering (Fig. 2d1 and e1), the width shrinkages of the struts of the Mg-Zn and pure Mg scaffolds were measured to be 11.2 ± 3.2% and 10.2 ± 2.3%, respectively

Table 1
Morphological characteristics of the Mg-Zn and pure Mg scaffolds fabricated by using the extrusion-based AM technique.

Sample group	Strut width (μm)	Strut spacing (μm)	Porosity in the struts after sintering	Absolute porosity
Design	580	360	–	37.8%
As-printed Mg-Zn	581.2 ± 14.9	343.9 ± 18.5	–	58.3 ± 1.6%
As-printed Mg	587.6 ± 11.7	351.4 ± 18.5	–	60.0 ± 1.9%
As-sintered Mg-Zn	516.1 ± 15.3	331.7 ± 39.5	6.9 ± 1.0%	50.3 ± 3.4% (W) 49.4 ± 5.7% (μCT)
As-sintered Mg	528.1 ± 12.6	298.4 ± 16.6	8.5 ± 0.4%	54.5 ± 2.4% (W) 52.3 ± 2.9% (μCT)

(Table 1). The total porosity of the sintered Mg-Zn scaffolds (50.3 ± 3.4% from the weighing method and 49.4 ± 5.7% from the μCT analysis) was lower than that of the sintered pure Mg scaffolds (54.5 ± 2.4% from the weighing method and 52.3 ± 2.9% from the μCT analysis). In the close-up views of the struts, sintering necks and open micropores could be observed between Mg-Zn or pure Mg powder particles (Fig. 2d2 and e2). The micropores inside the struts were more clearly seen when examining the cross-section microstructure (Fig. 2d3 and e3). From the MIP analysis, the micropores were found to be mostly in a size range of 2 - 10 μm, centered at around 5 μm (Fig. 2f). The lower cumulative intrusion volume of the Mg-Zn scaffolds (the inset in Fig. 2f) indicated fewer micropores in their struts, as compared to those of the pure Mg scaffolds, which is consistent with the calculated micro-porosities based on the cross-section microstructures of the struts (Table 1).

The etched Mg-Zn specimen showed a grain size of 26.5 ± 3.5 μm with second phase particles dispersing at grain boundaries (Fig. 2d4), while the etched pure Mg specimen exhibited a grain size of 28.3 ± 1.2 μm with clean grain boundaries (Fig. 2e4). Based on the XRD analysis, the as-sintered Mg-Zn scaffolds consisted of the α-Mg phase and $MgZn_2$ second phase, while only α-Mg phase was detected in the as-sintered pure Mg scaffolds (Fig. 2g).

3.2. In vitro *biodegradation behavior*

The Mg-Zn scaffolds maintained their structural integrity for the entire 28 days of immersion in the r-SBF solution with white biodegradation products gradually forming on their surface, while the pure Mg scaffolds lost most of their peripheral parts after 1 day of immersion (Fig. 3a). The pH changes in the proximity of the scaffold sample (*i.e.,* local pH) and further away (*i.e.,* distant pH) were measured (Fig. 3b). At the initial stage of the immersion, the local pH of both Mg-Zn and pure Mg exhibited fluctuations (see the arrows in Fig. 3b), while the distant pH increased steadily. During the first 24 h of immersion, the pH values associated with the pure Mg increased from 7.4 to around 9.5 with the local pH being higher than the distant one most of the time. The local pH value associated with the pure Mg specimens sharply increased to 9.3 during the first 10 h of immersion and tended to stabilize thereafter (Fig. 3b). By comparison, the pH values associated with the Mg-Zn remained lower than 8.0 during the first 24 h of immersion, with the local pH being only slightly higher than the distant one (Fig. 3b). The increase of the pH value associated with the Mg-Zn specimens slowed down after 10 days of immersion (Fig. 3c). The release of Mg ions from pure Mg was about twice as much as that from Mg-Zn during the first 24 h of immersion, while higher amounts of Ca and P ions were detected in the r-SBF solution of the Mg-Zn group (Fig. 3d). Throughout 28 days of immersion, the amount of Mg ions released from the Mg-Zn scaffolds increased from 141.3 ± 13.0 mg/L at day 1 to 359.3 ± 54.8 mg/L at day 28 (Fig. 3e). Over this period, the amounts of remaining Ca and P ions decreased. According to the μCT analysis, up to 28 days of immersion, the interspacing between the struts of the Mg-Zn scaffolds exhibited a gradual ascending trend (Fig. 3f). After segmenting the images of the Mg-Zn scaffolds (excluding the corrosion products), the volume loss of the Mg-Zn scaffolds was found to have increased from 7.1 ± 2.0% after 1 day of immersion to 64.6 ± 2.8% after 28 days of immersion (Fig. 3g). The volume loss of the pure Mg scaffolds has been found to be 37.3 ± 6.7% after 1 day of immersion [19], which is close to that of Mg-Zn after 7 days of immersion (the dash line in Fig. 3g). The average *in vitro* corrosion rate of the Mg-Zn scaffolds decreased from 2.3 ± 0.9 mm/y after 1 day of immersion to 0.7 ± 0.1 mm/y after 28 days of immersion (Fig. 3h). In the case of the pure Mg scaffolds, the corrosion rate reached 12.1 ± 0.2 mm/y after 1 day. When including the corrosion products during the segmentation of Mg-Zn scaffolds, the volume of the specimens was found to increase until day 7, and subsequently decreased (Fig. 3i). Once the corrosion products were segmented apart from the Mg-Zn substrate, the porosity of the Mg-Zn scaffolds gradually increased from an initial value of 49.4 ± 5.7% to 80.0 ± 0.6% after 28 days of immersion. By comparison, the porosity of the Mg-Zn scaffolds with the corrosion products decreased to 33.4 ± 7.1% at day 1 and further decreased to 24.0 ± 3.5% at day 3 (Fig. 3j). Then, the porosity remained stable until day 14 and subsequently increased at day 28 (Fig. 3j).

3.3. Characteristics of biodegradation products on the scaffolds

3.3.1. Chemical characteristics of the scaffold surface

FTIR revealed the presence of hydroxide (OH^-) and carbonates (CO_3^{2-}) on the surface of the biodegraded pure Mg

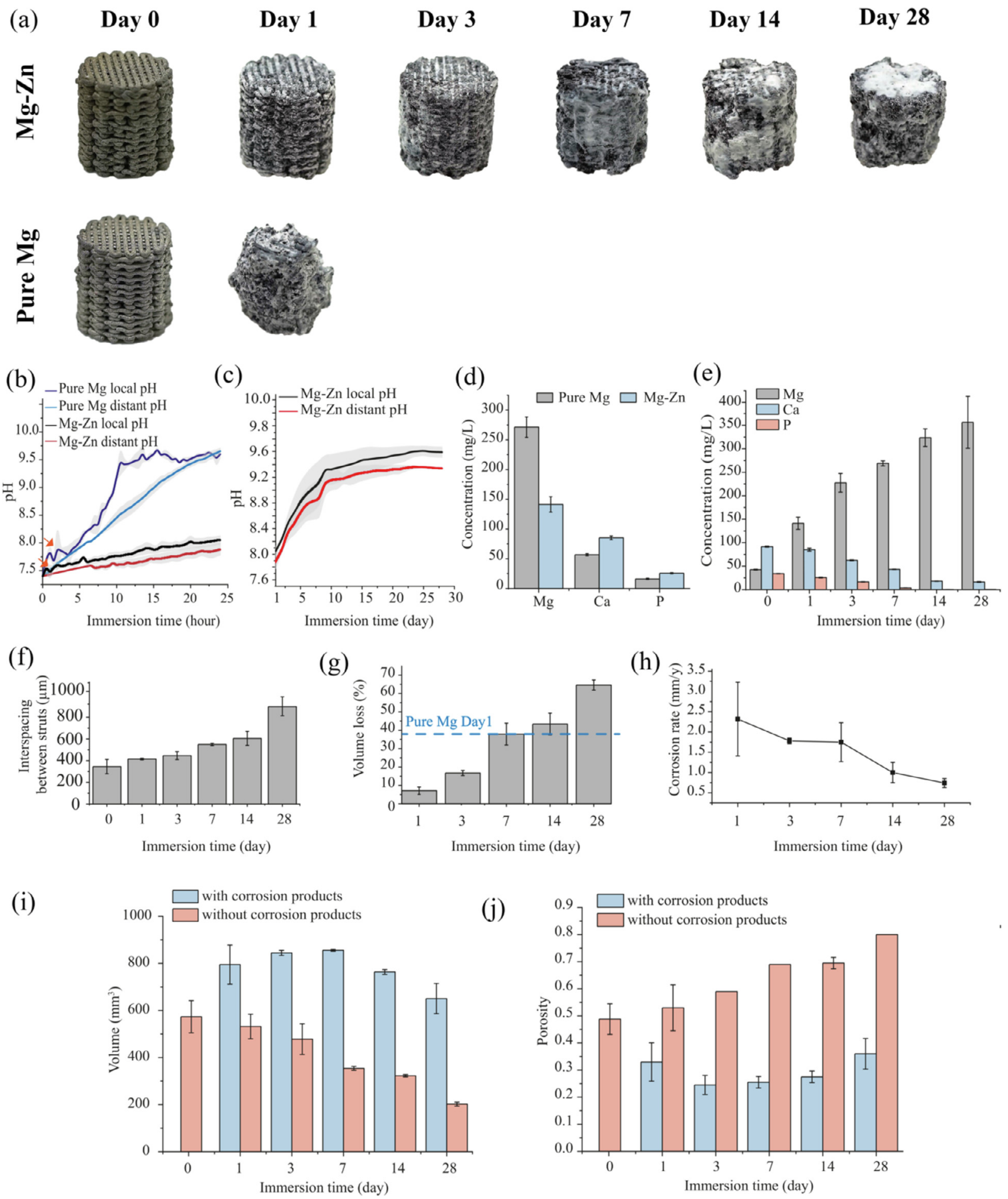

Fig. 3. *In vitro* biodegradation characteristics of the Mg-Zn scaffolds in comparison with those of the pure Mg scaffolds: (a) visual inspection of degraded scaffolds over immersion time, (b) pH variations during the first day of immersion, (c) pH variations up to 28 days of immersion, (d) changes of the concentrations of ions in r-SBF during the first day of immersion, (e) changes of the concentrations of ions in r-SBF up to 28 days of immersion, (f) changes of the interspacing between the struts of the degraded Mg-Zn scaffolds with immersion time, (g) volume loss over time, (h) calculated corrosion rates of the Mg-Zn scaffolds over time, (i and j) changes of the volume and porosity of the degraded Mg-Zn scaffolds with and without the corrosion products with immersion time. The results of pure Mg are cited from [18].

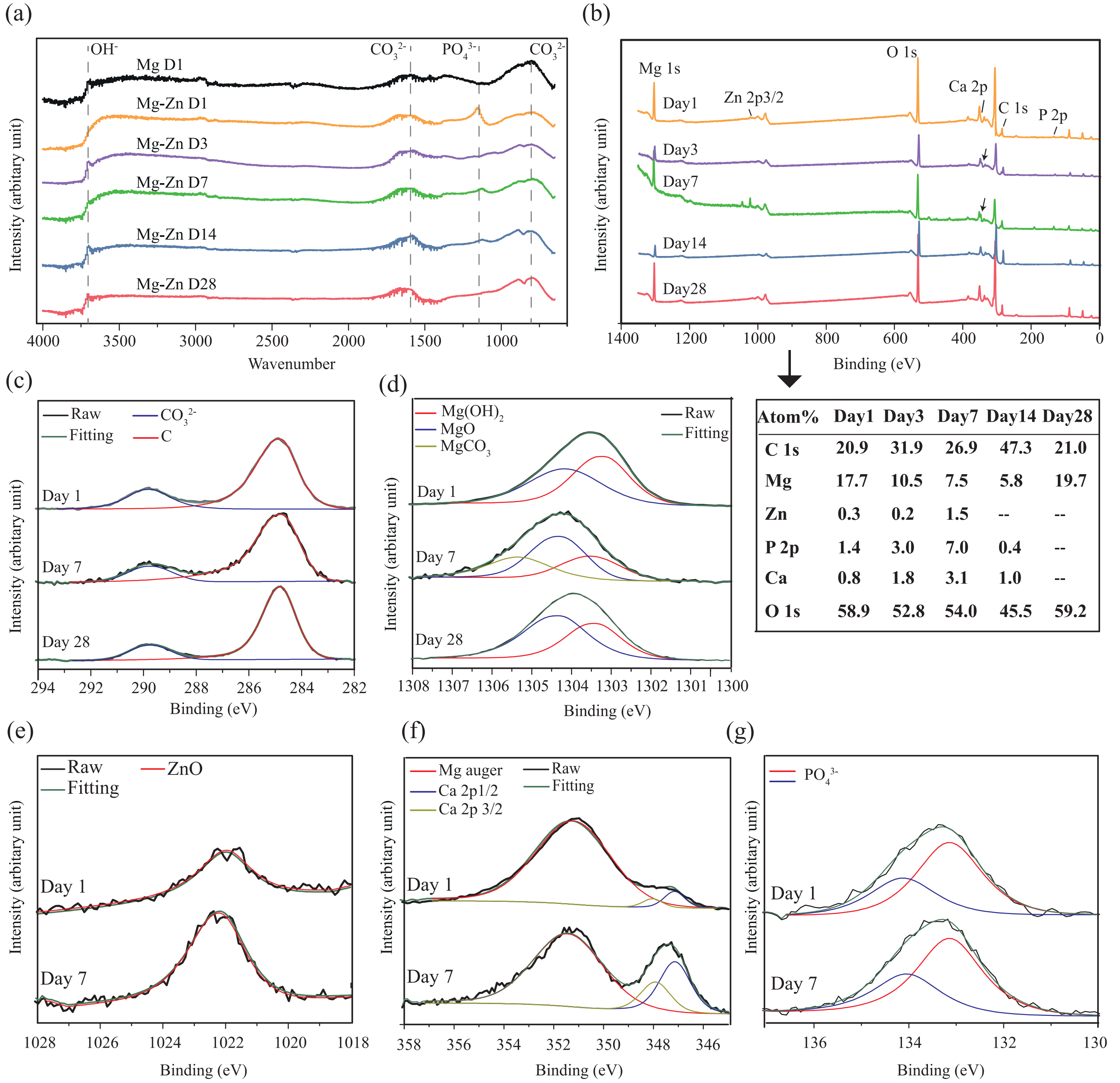

Atom%	Day1	Day3	Day7	Day14	Day28
C 1s	20.9	31.9	26.9	47.3	21.0
Mg	17.7	10.5	7.5	5.8	19.7
Zn	0.3	0.2	1.5	--	--
P 2p	1.4	3.0	7.0	0.4	--
Ca	0.8	1.8	3.1	1.0	--
O 1s	58.9	52.8	54.0	45.5	59.2

Fig. 4. Characteristics of the biodegradation products on the surface of Mg-Zn scaffold struts: (a) FTIR spectra (the spectrum of pure Mg after the first day of immersion cited from [18]), and (b-g) XPS spectra.

scaffolds with the following characteristics: OH^- absorption band at 3700 cm^{-1} [37] and CO_3^{2-} bands between 750-900 cm^{-1} and 1400–1550 cm^{-1} [38, 39]. By comparison, during the first day of immersion, the phosphates (PO_4^{3-}) with the absorption peak at around 1100 cm^{-1} emerged on the degraded Mg-Zn scaffolds with the appearance of CO_3^{2-} (Fig. 4a). However, the absorption peak of PO_4^{3-} decreased with the immersion time and disappeared after 28 days of immersion (Fig. 4a). XPS further revealed the compositional changes of the biodegradation products on the surface of the Mg-Zn scaffolds with the immersion time (Fig. 4b). The total XPS spectrum showed that the biodegradation products were composed of C, Mg, Zn, P, Ca, and O after 1 day of immersion. The percentage of Mg decreased until 14 days and sharply increased at day 28, while the percentages of Zn, P, and Ca increased first, started to decrease from day 14, and became too low to be detected at the end of the immersion period (Fig. 4b). Furthermore, the high-resolution XPS spectra of C1s, Mg1s, Zn2p3/2, Ca2p, and P2p were collected from the surfaces of the specimens (after *in vitro* biodegradation for 1, 7, and 28 days) and were then fitted (Fig. 4c-g). The peaks located at 285 and 290 eV may be due to hydrocarbon contamination and CO_3^{2-}, respectively (Fig. 4c) [40]. The peaks at 1303, 1304, and 1305 eV corresponded to $Mg(OH)_2$, MgO, and $MgCO_3$, respectively (Fig. 4d) [41], while the peak located at 1022 eV was attributed to ZnO (Fig. 4e) [1]. The Ca 2p peak consisted of Ca 2p1/2 at 348 eV and Ca 2p 2/3 at 347 eV, and a Mg Auger peak at 351 eV was also present in this region (Fig. 4f) [42]. The P2p peaks observed at about 133 and 134 eV (Fig. 4g) could be assigned to PO_4^{3-}. ZnO, Ca^{2+}, and PO_4^{3-} were observed on the surfaces of the specimens after 1 day and 7 days of immersion, but they could not be detected any more after 28 days of immersion (Fig. 4e-g).

3.3.2. Morphological characteristics

The original struts of the pure Mg scaffolds could not be recognized after only 1 day of immersion and their surfaces became completely covered by the biodegradation products (Fig. 5a1). The corrosion product layer with cracks consisted of C, O, Mg, and a minor amount of Ca (Fig. 5a2). At the center of the scaffolds, the space between the struts was filled with the biodegradation products (Fig. 5a3). The pure Mg struts were mostly replaced by the biodegradation products (Fig. 5a4) composed of Mg and O [19]. By comparison, the struts of the Mg-Zn scaffolds were still clearly visible after 1 day of immersion (Fig. 5b1) with a biodegradation product layer composed of C, O, Na, Mg, Zn, P, and Ca deposited on the struts (Fig. 5b2). The cross-section microstructure of the Mg-Zn scaffolds after 1 day of immersion showed the structural integrity of the struts and the interspacing between the struts were still well maintained (Fig. 5b3). The biodegradation products were formed within the initial interconnected pore network of the porous structure (Fig. 5b4). At day 3, both the struts and the space between the struts were covered by a thick deposition layer (Fig. 5c1). Flake-shaped products were formed on the surface, which contained C, O, Mg, Zn, and Ca (Fig. 5c2), while the space between the struts at the center of scaffolds were partially filled with the biodegradation products (Fig. 5c3). It was also observed that the struts corroded locally and the corroded areas were replaced by the biodegradation products (Fig. 5c3 and c4). At day 7, the biodegradation products on the surface were loose and porous (Fig. 5d1). Some needle-shaped crystals had also formed on the surface, in which Mg, O, Ca, and Cl were detected (Fig. 5d2). At the center of the scaffolds, after 7 days of immersion, the struts were further corroded, and dense biodegradation products had formed and fully filled the space between the struts (Fig. 5d3), closely surrounding the remaining struts (Fig. 5d4). At day 14, the surface of the scaffolds showed a bumpy morphology, instead of the original porous features (Fig. 5e1), and many bump-shaped corrosion products, containing C, O, Mg, and Ca, had appeared on the top of the former deposition layer (Fig. 5e2). At this time point, most of the struts were corroded with a few struts retaining their integrity (Fig. 5e3 and e4). After 28 days, a relatively dense and compact layer with a fish-scale-like structure was formed (Fig. 5f1), in which Ca had disappeared, while C, O, Mg, and a trace amount of Na were detected (Fig. 5f2). The biodegradation products at the center of the scaffolds were more porous (Fig. 5f3 and f4). In order to reveal the compositions of the biodegradation products formed at the center of the scaffolds, EDS mapping analysis was performed on the scaffolds after 14 days of immersion, showing that Mg and O were the main elements with some trace amounts of Ca, P, C and Zn.

3.4. Electrochemical response

The Mg-Zn and pure Mg scaffolds exhibited similar anodic and cathodic polarization behaviors. However, Mg-Zn exhibited a nobler corrosion potential (E_{corr}) and a lower current density (i_{corr}) than those of pure Mg (Fig. 6a). The current density values of Mg-Zn and pure Mg were respectively $4.3•10^{-5} \pm 0.9•10^{-5}$ and $9.6•10^{-5} \pm 1.7•10^{-5}$ $A•cm^{-2}$, corresponding to corrosion rates of 1.1 ± 0.8 and 2.2 ± 0.0 mm/y. The LPR values of the Mg-Zn scaffolds decreased from 2.1 ± 0.4 $KΩ•cm^2$ to 1.1 ± 0.2 $KΩ•cm^2$ during the first 3 days of immersion, and then increased to 2.2 ± 0.1 $KΩ•cm^2$ until day 14, followed by a decrease at day 21 (Fig. 6b). As compared with Mg-Zn, the LPR values of the pure Mg scaffolds remained at a very low level during the first day of immersion (around 0.5 $KΩ•cm^2$).

3.5. Mechanical properties

The uniaxial compressive stress-strain curves of the Mg-Zn and pure Mg scaffolds both began with a linear elastic region, followed by densification during the plastic deformation stage until failure (Fig. 7a). The yield strength and elastic modulus of the Mg-Zn scaffolds (14.5 ± 3.0 MPa and 448.8 ± 42.4 MPa, respectively) were much higher than those of the pure Mg scaffolds (4.7 ± 0.7 MPa and 184.4 ± 37.3 MPa, respectively). The biodegraded specimens showed a notable decline in their strain to failure from 30 ± 8% prior to the *in vitro* immersion to 16 ± 1% after 14 days of immersion (Fig. 7b). Over the *in vitro* immersion period, the yield strength of the scaffolds markedly increased from 14.5 ± 3.0 MPa before degradation to 34.9 ± 7.3 MPa after 3 days of immersion and then declined to 24.6 ± 7.6 MPa at day 14 (Fig. 7c). Likewise, the elastic modulus increased from 448.8 ± 42.4 MPa to 735.9 ± 220.6 MPa at day 3 and then decreased to 282.9 ± 83.6 MPa after 14 days of immersion (Fig. 7d).

3.6. In vitro *biological evaluation of the scaffolds*

The exposure of MC3T3-E1 cells to the 100% extracts of the Mg-Zn and pure Mg scaffolds led to instant cytotoxicity (Fig. 8a). When the extracts were diluted to 50%, a low metabolic activity of 24.0 ± 6.6% was detected for the Mg-Zn group, which decreased until day 7, while the pure Mg group showed a higher metabolic activity of 84.8 ± 12.8% after 1 day of culture, which was maintained until 7 days of cell culture. When the extracts were further diluted to 10%, however, the metabolic activity of the Mg-Zn and

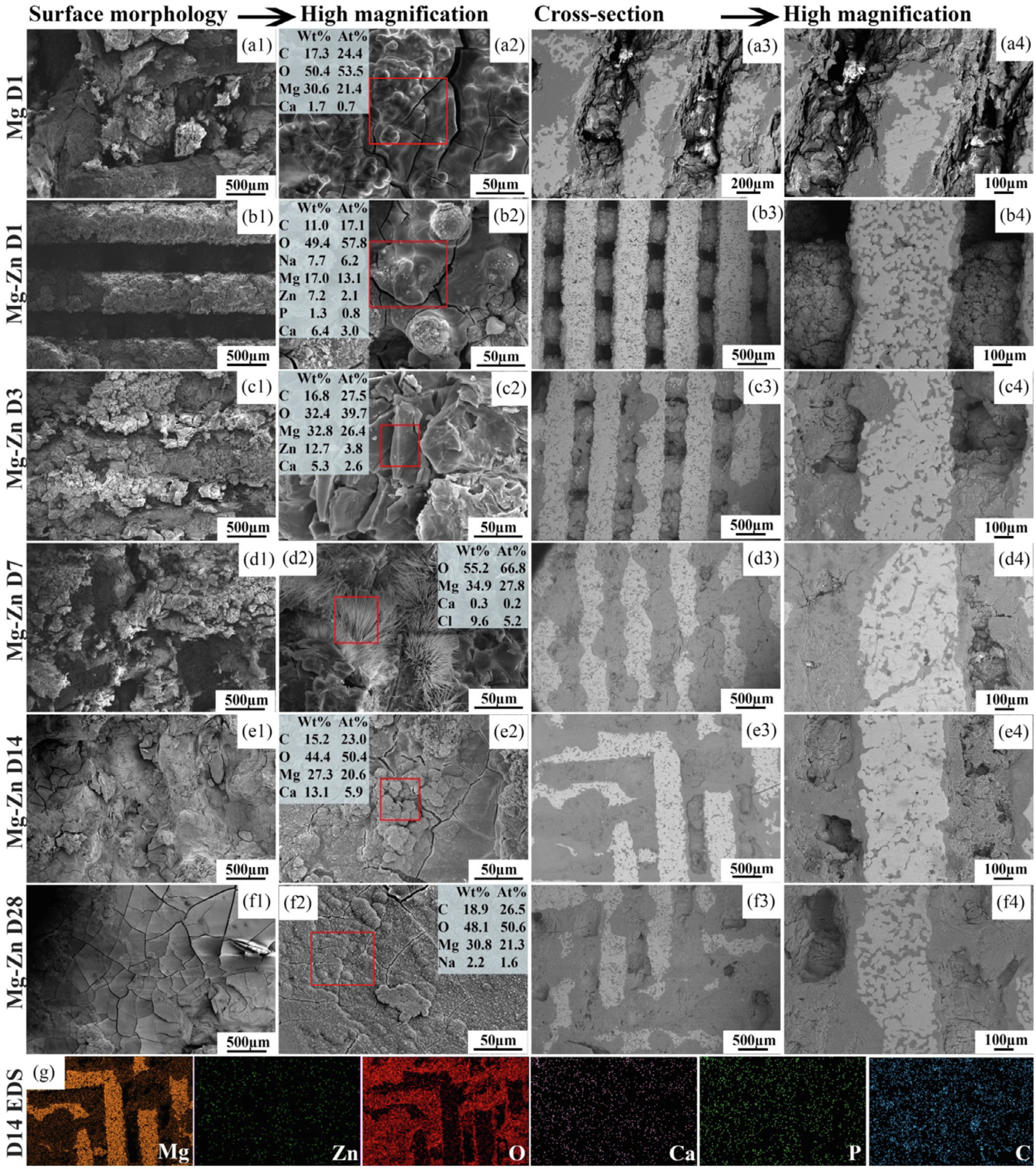

Fig. 5. SEM images of the biodegradation products on the scaffold outer surfaces and in the center of the Mg-Zn scaffold in comparison with those of the pure Mg scaffolds: (a1-a4) pure Mg scaffolds after 1 day of immersion, (b1-b4) Mg-Zn scaffolds after 1 day of immersion, (c1-c4) Mg-Zn scaffolds after 3 days of immersion, (d1-d4) Mg-Zn scaffolds after 7 days of immersion, (e1-e4) Mg-Zn scaffolds after 14 days of immersion, (f1-f4) Mg-Zn scaffolds after 28 days of immersion, and (g) EDS analysis of the Mg-Zn scaffolds after 14 days of immersion. The boxed area and values indicate the spots where the EDS analyses were performed and the corresponding elemental compositions, respectively.

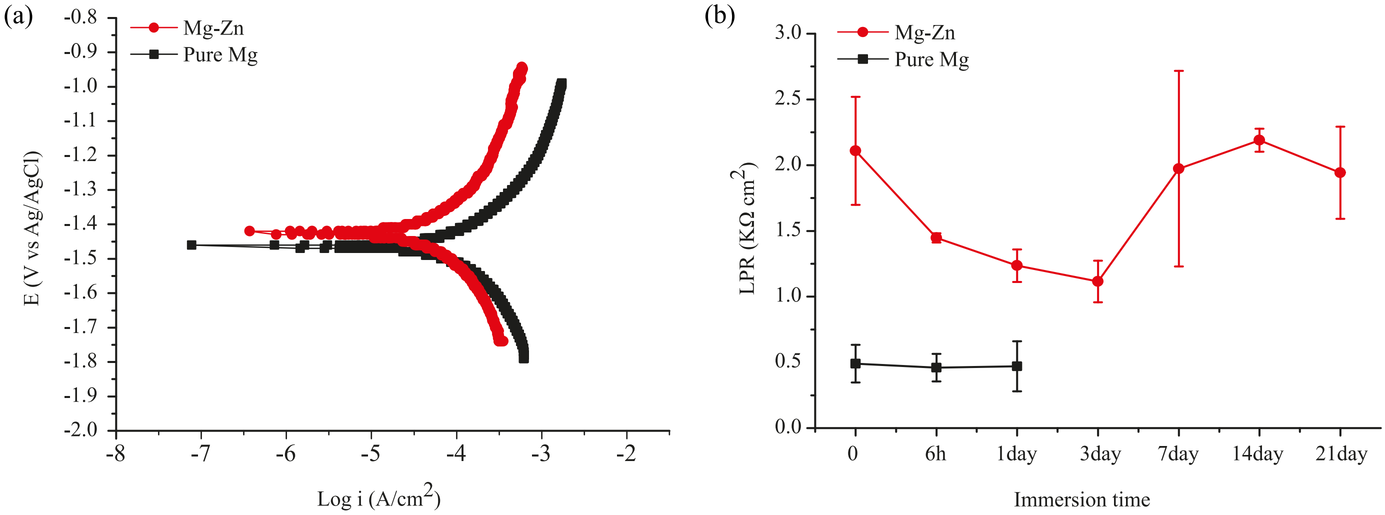

Fig. 6. Electrochemical test results: (a) Potentiodynamic polarization after 1 h of exposure, and (b) linear polarization resistance over a period of 21 days of exposure for the bare Mg and Mg-Zn scaffolds. The results of pure Mg are cited from [18].

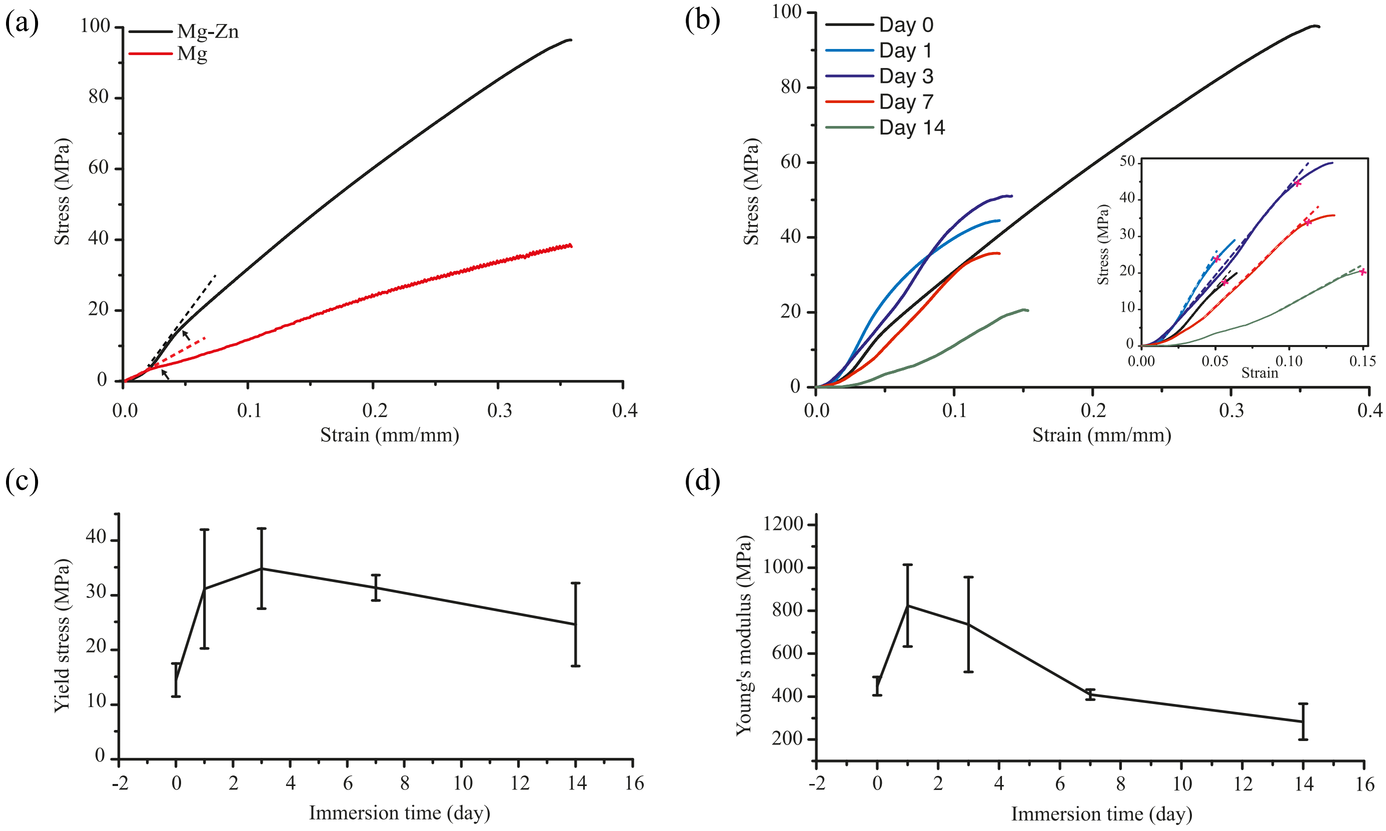

Fig. 7. Compressive mechanical properties of the Mg-Zn scaffolds in comparison with those of the pure Mg scaffolds: (a) stress-strain curves of the scaffolds before *in vitro* biodegradation (the curve of pure Mg cited from [18]), (b) stress-strain curves of the degraded Mg-Zn scaffolds, (c) variation of yield strength with immersion time, and (d) variation of Young's modulus with immersion time. Dash lines in the insets indicate the linear regions; arrows and crosses indicate the yield strengths.

pure Mg groups stayed at high levels (> 90%) until 7 days of cell culture (Fig. 8a). The pH values of the 10% extracts of the Mg-Zn and pure Mg scaffolds were only marginally lower than those of the corresponding 50% and 100% extracts (Fig. 8b). However, lower concentrations of Mg ions were found in the diluted extracts of both Mg-Zn and pure Mg (Fig. 8c). In addition, the concentrations of Mg ions in the 50% and 100% Mg-Zn extracts were lower than those in the 50% and 100% pure Mg extracts (Fig. 8c). The concentration of Zn ions released from the Mg-Zn scaffolds decreased with

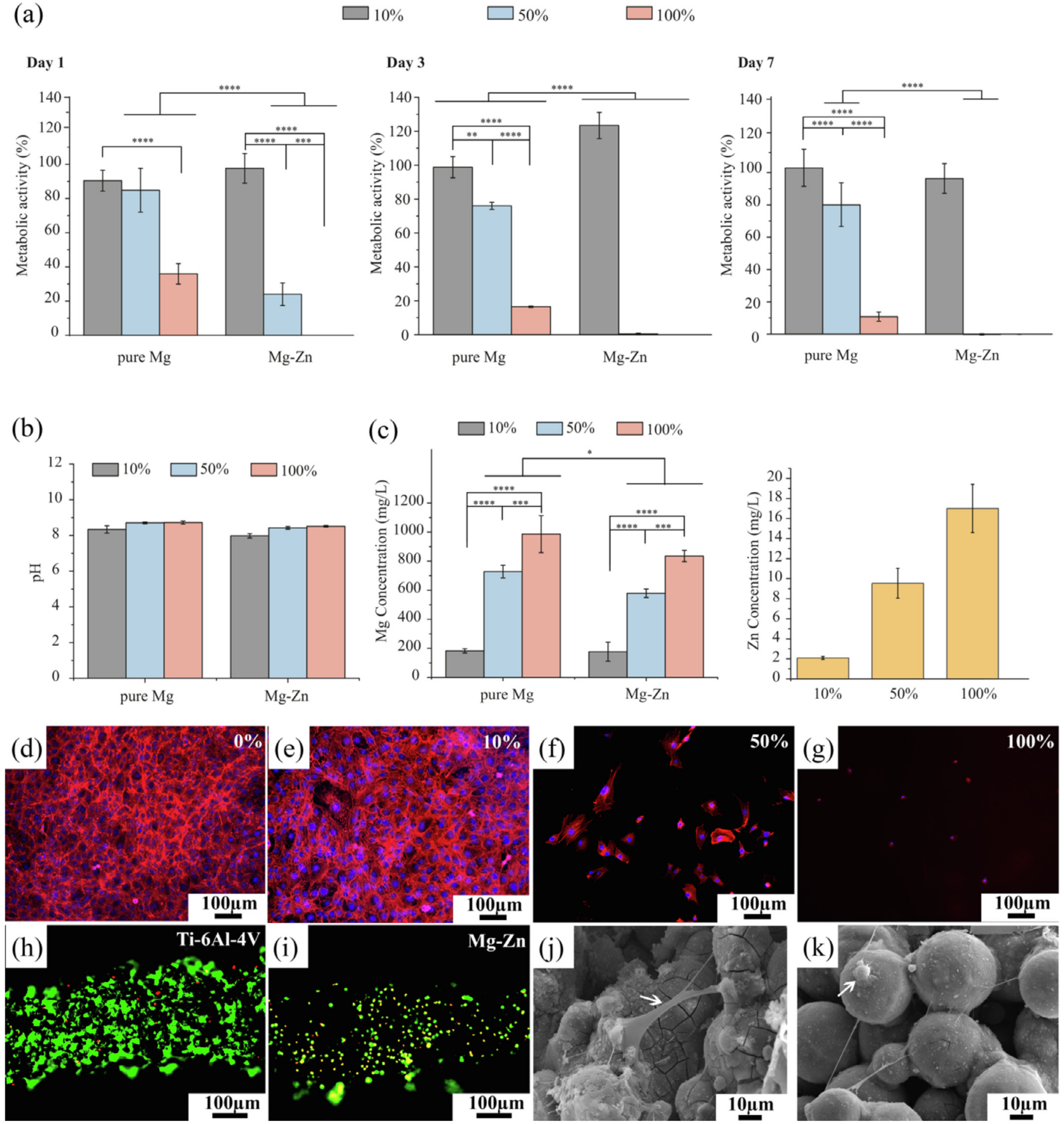

Fig. 8. *In vitro* biological evaluation of the scaffolds: (a) indirect metabolic activity values of preosteoblasts cultured in the 10%, 50% and 100% extracts of the Mg-Zn and pure Mg scaffolds [18], (b-c) pH and ion concentrations of the Mg-Zn and pure Mg [18] extract media of different concentrations, (d-g) rhodamine phalloidin (red) and DAPI (blue) stained preosteoblasts after 3 days of culture in the 0%, 10%, 50% and 100% extracts of the Mg-Zn scaffolds, (h-i) calcein acetoxymethyl (green, indicating living cells) and ethidium homodimer-1 (red, indicating dead cells) stained preosteoblasts on the Mg-Zn scaffolds (with Ti-6Al-4V as the reference), and (j-k) the morphologies of cells on the Mg-Zn scaffolds after 3 days of direct cell culture.

increasing dilution ratio of the extracts (17.0 ± 2.4 mg/L in the 100% extract and 2.1 ± 0.1 mg/L in the 10% extract) (Fig. 8c). When cultured in the 10% Mg-Zn extracts for 3 days, the cells formed a confluent layer and showed a spread morphology with well-developed stress fibers (Fig. 8e), similar to the control group (0% extract, *i.e.,* the α-MEM medium) (Fig. 8d). However, only a few cells could be observed in the 50% Mg-Zn extracts (Fig.8f) and they presented a less spread morphology. In the 100% Mg-Zn extracts, there were hardly any cells (Fig. 8g).

In the direct cell culture, the preosteoblasts showed a homogenous distribution over the struts of the Mg-Zn scaffolds after 3 days with the presence of both viable and unhealthy/dead preosteoblasts (Fig. 8i). The cells were also less spread as compared to the cells grown on the reference Ti6Al4V scaffolds (Fig. 8h). SEM imaging of the Mg-Zn scaffolds after 3 days of culture revealed that some cells could spread between the cluster of particles (the arrows Fig.8j) whereas others settled on such clusters adopting a round morphology (the arrows in Fig. 8k).

4. Discussion

In this research, extrusion-based AM was employed to fabricate geometrically-ordered pre-alloyed Mg-Zn scaffolds, which had not been demonstrated before. Upon heating, the Mg-Zn binary alloy was brought into the solid-liquid two-phase region between the solidus and liquidus [43], thus having a broader sinterability window than pure Mg. Therefore, a specific sintering scheme was first developed for the fabrication of the Mg-Zn scaffolds. The fabricated Mg-Zn scaffolds with denser struts and the dispersed second phase contributed to the improved mechanical properties and corrosion resistance, as compared to those of the pure Mg scaffolds. In addition, the indirect culture of preosteoblasts in the Mg-Zn extracts with the recommended dilution ratio (6–10 times [44]) revealed good biocompatibility.

4.1. Fabrication of the mg-zn scaffolds

The extrusion-based AM technique enabled precise printing of the Mg-Zn and pure Mg scaffolds with strut sizes and strut spacing values close to the design values (Table 1). A single-step debinding and sintering process was applied to the as-printed Mg-Zn scaffolds. The sintering step of the Mg-Zn scaffolds was, however, different from the one applied to pure Mg in our previous studies [18]. The existence of the liquid-solid two-phase region for the Mg-Zn alloy allowed for the variation of the density of the struts by controlling the volume fraction of the liquid phase formed during sintering, which was infeasible for pure Mg due to the absence of such a liquid-solid two-phase region. To determine a suitable range of the sintering temperatures, the dependence of liquid phase fraction on temperature was calculated based on the thermodynamic equilibrium (Fig. S1). In conventional powder metallurgy, an optimum fraction of the liquid phase for liquid-phase sintering is reportedly between 5 and 15 vol% and the higher fraction of the liquid phase, the higher density of struts could be achieved within a shorter sintering time [45]. Therefore, a sintering temperature range of 570 to 590 °C was selected, corresponding to a liquid fraction range of 10–15 vol% for the Mg-Zn alloy with 4 wt% Zn. The optimization of the sintering scheme was based on the measured density of the struts and the fidelity of the Mg-Zn scaffolds (Fig. S2). Although a higher temperature (590 °C/1 h) was beneficial for the densification of Mg-Zn scaffold struts (Fig. S2-a), the fidelity of the scaffolds was diminished due to the formation of nodules at the peripheral struts (the arrow in Fig. S2-d). This was also observed during the optimization of the sintering scheme for pure Mg [18]. To ensure that a similar level of porosity could be achieved and to avoid an unexpected increase in grain size, sintering with a dwelling time of 1 h was selected for the Mg-Zn scaffolds (the same as for pure Mg). Based on the preceding studies, the optimized sintering parameters of 580 °C/1 h and 640 °C/1 h [19] were used for the sintering of the Mg-Zn and Mg scaffolds, respectively. After the post-processing, both the Mg-Zn and pure Mg scaffolds possessed a hierarchical porous structure with macropore sizes of about 300 μm and micropore sizes of < 100 μm in the struts (Table 1 and Fig. 2), which could be favorable for the adhesion, proliferation, and differentiation of cells [46]. Under the premise of guaranteeing fidelity, the fabricated Mg-Zn scaffolds exhibited a slightly higher density in the struts and, thus, lower porosity of the whole structure than the pure Mg scaffolds (Fig. 2f and Table 1).

The precipitated $MgZn_2$ second phase was found in the Mg-Zn scaffolds (Fig. 2d4) due to the low solubility of Zn (1.6 wt%) in the α-Mg phase at room temperature [43], which has been also reported in some other studies on Mg-Zn alloys [21, 47]. The mean grain size of the original Mg-Zn powder (2.8 ± 0.1 μm) was smaller than that of the pure Mg powder (8.6 ± 1.7 μm), which could be attributed to the grain-refining effect of Zn [27, 48]. However, this effect was not clearly visible any more after sintering, as evidenced by the similar grain sizes of the sintered Mg-Zn and pure Mg scaffolds (about 30 μm).

4.2. In vitro *biodegradation behavior*

The static *in vitro* corrosion resistance of the Mg-Zn scaffolds was significantly better than that of the pure Mg scaffolds (Table 2). Comparisons in pH value, the concentration of Mg ion, and volume loss after 1 day of immersion all clearly showed that the fabricated Mg-Zn scaffolds had much improved corrosion resistance (Fig. 3). Similar remarkable improvements in the corrosion resistance have been observed in other studies on the cast and powder metallurgy Mg-Zn binary alloys [21, 22]. The improved corrosion resistance of the Mg-Zn scaffolds could be attributed to the addition of Zn, which elevates the corrosion potential of Mg (Fig. 6a) [22, 23]. Although the presence of second phase particles could cause micro-galvanic corrosion, the corrosion of our Mg-Zn alloy with < 5 wt% Zn was not dominated by micro-galvanic corrosion, since with a low Zn content, second phase particles are dispersed in the α-Mg matrix (Fig. 2d4) instead of forming a continuous network structure that could lead to widespread and distinct anode-cathode sites [22]. In addition, Zn can increase the tolerance limits of impurities, thereby reducing the corrosion rate of Mg [49]. Moreover, many other researchers [23, 50-53] have found that the addition of Zn to Mg can accommodate the formation of a compact corrosion product film. When a Mg-Zn alloy is exposed to the r-SBF solution,

Table 2
Comparison between the *in vitro* biodegradation rates of the Mg-Zn scaffolds and those of the same alloy in other studies.

Material	Fabrication technique	Porosity	Grain size (μm)	In vitro degradation rate (mm/y)	Medium	Ref.
Mg-4Zn	cast	0%	–	day 6: 2.1	c-SBF	[52]
Mg-4Zn	cast	0%	100	day 7: 4.3 day14: 3.4	c-SBF	[55]
Mg-4Zn	cast + extrusion	0%	11.2	day 7: 1.9	PBS	[56]
Mg-4Zn	cast + extrusion	0%	14.5	day 10: 3.7	PBS	[57]
Mg-4Zn	powder metallurgy	0.9%	23.2	day 1: 2.5	3.5% NaCl	[21]
Mg-4Zn	extrusion-based AM	50.3 ± 3.4%	26.5	day 1: 2.3 ± 0.9 day 7: 1.7 ± 0.5 day 14: 1.0 ± 0.3 day 28: 0.7 ± 0.1	r-SBF	this study
Pure Mg	extrusion-based AM	54.5 ± 2.4%	28.3	day 1: 12.1 ± 0.2	r-SBF	this study
Ideal bone substitute	–	–	–	0.2 – 0.5	–	[58]

the alloy surface is oxidized to generate Mg^{2+} and Zn^{2+} ions and, at the same time, OH^- and H_2 are produced by the reduction of H_2O. The Mg^{2+} and Zn^{2+} react with OH^- to form $Mg(OH)_2$ and $Zn(OH)_2$ as a layer of precipitates on the alloy surface. It is well known that, in the r-SBF solution, $Mg(OH)_2$ is vulnerable to Cl^- attack, leading to the formation of soluble $MgCl_2$. However, $Zn(OH)_2$ is known to be transformed into stable ZnO at the very early stage of immersion (within 300 s), contributing to the formation of a protective corrosion film on the surface of the Mg-Zn alloy [51]. Therefore, during the first day of immersion, ZnO compounds appeared on the surface of the Mg-Zn scaffolds (Fig. 4e), providing a more stable film than the one present on the surface of pure Mg, which was preferable for the deposition of calcium phosphate products. This could explain why after 1 day of immersion, PO_4^{3-} was formed on the Mg-Zn scaffolds but not on the pure Mg scaffolds (Fig. 4a). The calcium phosphate phase that is similar in composition to the inorganic phase of the bone can be utilized by osteoblasts to form new bone [54].

The static *in vitro* biodegradation rate of the Mg-Zn scaffolds presented here was compared with the values of bulk and foam Mg-Zn alloys fabricated by conventional techniques (Table 2) [52, 55-57] and with the desired rates of biodegradation. We found that the biodegradation rate of the Mg-Zn scaffolds (0.7 ± 0.1 mm/y at day 28) developed here is quite close to the biodegradation rate of an ideal bone substitute (0.2 - 0.5 mm/y) [58]. In addition, the corrosion rate (1.7 ± 0.5 mm/y at day 7) of our Mg-Zn scaffolds is similar to cast and extruded Mg-Zn alloys (with 4 wt% Zn) (1.9 - 4.3 mm/y at day 7, Table 2). The fabricated Mg-Zn scaffolds with a porosity of around 50% had an initial biodegradation rate of 2.3 ± 0.9 mm/y, which is similar to the biodegradation rate of the Mg-Zn alloy (4 wt% Zn, grain size = 23.2 μm) with 1% porosity fabricated through conventional powder metallurgy (Table 2). One of the reasons for such a remarkable corrosion resistance is the finer grains in our Mg-Zn scaffolds (26.5 ± 3.5 μm), especially when compared with that of bulk alloys in their as-cast condition (Table 2). Another important reason could be that the interconnected porous structure of our Mg-Zn scaffolds allowed stable ZnO to participate in the formation of the corrosion products everywhere, which helps in maintaining the integrity of the structure and effectively retards the progress of the corrosion process.

At the early stage of *in vitro* immersion, ZnO could be found on the surface of the Mg-Zn scaffolds accompanied by Mg $(OH)_2$, MgO, $MgCO_3$, and calcium and phosphate-containing precipitates (Fig. 4a and b). At the later stages of *in vitro* immersion (*i.e.*, day 14 and day 28), however, ZnO could not be detected any more on the surface of the specimens (Fig. 4b). This is likely because Zn is less chemically active, as compared to Mg. Mg is, therefore, preferentially oxidized and Mg-containing degradation products are formed on the surface first [52]. With time, thus, more and more Mg $(OH)_2$ or MgO are found in the outer layers of the biodegradation products, while ZnO is found in the inner layers. This trend has been also reported in other studies [52, 59]. In addition, the formed ZnO could facilitate the further formation of $Mg(OH)_2$ [53], leading to an increasingly dense degradation layer on the surface of the Mg-Zn scaffolds (Fig. 5b1-f1).

After 1 day of immersion, corrosion was found to have occurred both at the periphery and in the center of the struts. The biodegradation products formed on the peripheral struts and inside the initial micropores in the struts (Fig. 5b3-b4) led to a sharp increase in the total volume of the scaffolds (including the volume of the biodegradation products), but a decrease in porosity (Fig. 3i and j). With corrosion further progressing over time, the struts gradually became incomplete and stable degradation products continuously formed on the struts until the space between the struts was fully occupied (Fig. 5c3, d3 and e3). As a result, the porosity of the scaffolds (including the biodegradation products) was maintained at around 25% (Fig. 3j), and the volume of the scaffolds (including the biodegradation products) was higher than that of the initial scaffolds between days 3 and 14 (Fig. 3i). The biodegradation products present at the center of the scaffolds had a similar composition to those on the surface (Fig. 5g).

The compact and dense biodegradation products present on the surface and in the space between the struts generally hindered the further corrosion of the Mg-Zn scaffolds, hence reducing the corrosion rate from 2.3 ± 0.9 mm/y to 0.7 ± 0.1 mm/y over 28 days of immersion (Fig. 3h). The reduced corrosion rate was also reflected in the gradually stable pH values from day 7 (Fig. 3c), the minor changes of the volume and porosity of the Mg-Zn scaffolds (excluding the biodegradation products) between days 7 and 14 of immersion (Fig. 3i and j), and the increased LPR values at days 7 and 14 (Fig. 6b). It has been found that thanks to the formation of a stable degradation product layer on Mg-Zn alloy implants, the further *in vivo* corrosion is retarded, which makes the microenvironment more favorable for the establishment of osteointegration [30] .

4.3. Bone-mimicking mechanical properties

The uniaxial compressive stress-strain curves of both the Mg-Zn and pure Mg scaffolds exhibited two stages: (i) an initial elastic stage and (ii) a densification stage (Fig. 7a). Unlike other geometrically ordered 3D printed porous metallic scaffolds [60], the strain-stress curves of the Mg-Zn and pure Mg scaffolds studied here did not exhibit a plateau stage, which would normally be expected of a porous structure with a 0º to 90º lay-down pattern or 90º interconnection between struts [61]. In addition to the pattern, both macropores and micropores in the scaffolds contribute to the strain-hardening behavior observed during the plastic deformation stage [62].

The yield strength and elastic modulus of the Mg-Zn scaffolds were about three times as high as those of the pure Mg scaffolds (Fig. 7a). The significantly enhanced mechanical properties of the Mg-Zn scaffolds could be attributed to the combined effects of the material and the structure. From a material perspective, the compressive yield strength of the bulk Mg-Zn alloy (4 wt% Zn, 110 MPa [63]) is much higher than that of bulk pure Mg (21 MPa [64]). The maximum solubility of Zn in Mg is 1.6 wt% at room temperature in the equilibrium state. Part of Zn in the Mg-Zn alloy is, therefore, dissolved in the α-Mg matrix, generating solid-solution strengthening. The rest of Zn precipitates from the α-Mg matrix during cooling from the sintering temperature and constitutes the second phase dispersed along the grain boundaries, thereby strengthening the Mg-Zn alloy through a dispersion-strengthening mechanism [22]. In other words, both the solid-solution strengthening and dispersion strengthening mechanisms contributed to the improved mechanical properties of the Mg-Zn scaffolds.

For application as biodegradable metallic bone implants, the mechanical properties of Mg-Zn porous biomaterials should be maintained until the newly formed bone can take over the mechanical function from the implants and provide enough mechanical support. Therefore, understanding the evolution of the mechanical properties of scaffolds with biodegradation time is of great importance to avoid sudden premature failure. During the 28 days of *in vitro* biodegradation, the mechanical properties of our Mg-Zn scaffolds remained in the range of those of trabecular bone (*i.e.,* yield strength = 0.2 – 80 MPa; elastic modulus = 10 – 2000 MPa) [65]. The yield strength and elastic modulus of the Mg-Zn scaffolds were indeed influenced by *in vitro* biodegradation. The formation of the corrosion products, resulting in increased mechanical properties, and the dissolution of the Mg-Zn scaffolds, resulting in decreased mechanical properties, nicely balanced each other out (Fig. 3 and Fig. 5) [66]. Throughout the initial immersion period, the structure of the Mg-Zn scaffolds maintained its general integrity, suggesting that the corrosion products have likely played an important role in increasing the mechanical properties of the scaffolds. The yield strength and elastic modulus were measured at an initial deformation stage, when interfacial bonding between the Mg-Zn scaffolds and corrosion products was still good and the applied load could easily be transferred between the Mg-Zn scaffold and the corrosion products [66]. Moreover, the formation of the corrosion products filling the micropores inside the struts and covering the struts led to a sharp decrease in the porosity of the entire scaffolds (including the corrosion products, Fig. 3j), enabling them to withstand higher loads. Therefore, the corrosion products (*i.e.,* the inorganic compounds) effectively acted like a reinforcing phase in the Mg-Zn scaffolds, providing a strengthening effect [10], which explains why the yield strength and elastic modulus of the Mg-Zn scaffolds increased after 1 day of immersion (Fig. 7c and d). After 3 days of immersion, localized corrosion occurred (Fig. 5c3), which could lead to the generation of stress concentrations. In addition, the Mg-Zn scaffolds themselves could bear less loading, as the corrosion progressed. As a result, declining trends of the yield strength and elastic modulus were observed (Fig. 7c and d).

4.4. Characteristic responses of preosteoblasts

For both the Mg-Zn and pure Mg scaffolds, different dilution ratios of the extracts led to different levels of preosteoblast viability. According to the ISO 10,993–5 standard [67], the 100% extracts of both Mg-Zn and pure Mg were severely toxic (Level 4) after 7 days of cell culture. The 50% extract of Mg-Zn was also categorized as severely toxic (Level 4), while the 50% extract of pure Mg showed slight toxicity (Level 1). When the extracts of Mg-Zn and pure Mg were further diluted to 10%, about 100% metabolic cell activity was detected, showing no toxicity (Level 0). These effects of the dilution ratio of the extract on the growth of preosteoblasts were supported by the rhodamine-phalloidin and DAPI stainings (Fig. 8d-g).

The pH values of the extracts of the Mg-Zn and pure Mg scaffolds were all below 8.5, being lower than the pH tolerance threshold of MC3T3-E1 cells (pH = 8.8) [24]. Therefore, the release of ions was the primary factor determining the cytocompatibility of the scaffolds. It is well known that Mg ion promotes bone regeneration [68]. However, an excessively high Mg ion concentration can adversely affect cell proliferation [44]. A safe Mg ion concentration for MC3T3-E1 cells is less than 360 mg/L [44], which can explain the cytotoxic effects of the 50% and 100% extracts of Mg-Zn and pure Mg (Fig. 8a and c). As compared to the 50% and 100% extracts of pure Mg, the extracts of Mg-Zn had significantly less Mg^{2+} release (Fig. 8c), due to a lower biodegradation rate of the Mg-Zn scaffolds (Fig. 3). The cells cultured in these extracts, however, exhibited more severe toxicity than the pure Mg counterparts (Fig. 8a). This inhibitory effect on the growth of preosteoblasts could be attributed to the high Zn^{2+} concentration in the Mg-Zn extracts. Since the human body has a much greater demand for Mg than for Zn, Zn exhibits a more significant dose-dependent effect on cytocompatibility than Mg. A low concentration of Zn^{2+} has been found to promote the viability, proliferation, and migration of osteoblast cells, while a high concentration of Zn^{2+} has been shown to cause adverse effects [54]. The IC_{50} of Zn^{2+} (*i.e.*, the half maximal inhibitory concentration) is reported to be about 5.9 mg/L for MC3T3-E1 cells [69] with a safe limit of 3 mg/L [70, 71], which explains why the 50% (9.6 ± 1.5 mg/L) and 100% extracts (17.0 ± 2.4 mg/L) of Mg-Zn exhibited severe toxicity, while the 10% Mg-Zn extract was cytocompatible (2.1 ± 0.1 mg/L).

The *in vitro* biosafety evaluation of biodegradable Mg does not reflect the i*n vivo* situation where the circulating body fluid tends to decrease the local concentrations of Mg and Zn ions. In addition, the concentrations of detected Mg and Zn ions in the blood serum (*in vivo*) are reported to be much lower than those in the extracts (*in vitro*), and the cells in tissue (*in vivo*) and culture medium (*in vitro*) had different maximum tolerated doses of Mg and Zn ions [44, 54]. Considering these factors, 6–10 times dilution of the original extracts has been strongly recommended for the *in vitro* cytotoxicity tests of Mg to be developed as potential orthopedic implants [44]. Such a dilution ratio corresponds to the biocompatible Mg-Zn extracts (*i.e.*, 10% extracts) in the indirect assays performed here (Fig. 8a).

While our direct cell culture tests demonstrated a certain level of cytotoxicity for the Mg-Zn scaffolds (Fig. 8i) including unhealthy cells (Fig. 8k), a number of stretched cells with developed filopodia adhering well to the corrosion layer of the Mg-Zn scaffolds were also observed (Fig. 8j). Both the spreading and non-spreading morphologies of the MC3T3-E1 cells have also been observed on extruded Mg-Zn alloys (6 wt% Zn) [25]. Furthermore, it has been reported that such extruded Mg-Zn implants exhibit good *in vivo* biocompatibility [23, 72, 73], superior osseointegration due to a stable corrosion layer, and improved osteogenic differentiation of rBMCs cells [30]. In addition, the *in vivo* biodegradation of the extruded Mg-Zn implants (degradation rate: 2.32 mm/y) has not been found to be harmful to the adjacent bone tissues because the excess Mg^{2+} can be excreted by the kidney, while Zn^{2+} can be absorbed by the surrounding tissues and excreted through the gastrointestinal route and the kidney [23]. Therefore, it is important to realize that *in vitro* cytocompatibility assessment cannot completely mimic the *in vivo* conditions and comprehensive *in vitro* and *in vivo* studies are required to better understand the biological responses of cells to our scaffolds.

5. Conclusions

In this study, for the first time, biodegradable Mg-Zn alloy scaffolds were successfully fabricated through an extrusion-based AM technique and subsequent debinding and sintering. With the pure Mg scaffolds as the reference, the Mg-Zn scaffolds were comprehensively studied for their intended application as a biodegradable bone substitute.

1 The porous structure of the fabricated Mg-Zn scaffolds was interconnected, owing to the presence of macropores from the pattern design and the micropores formed in the struts.
2 The μCT results showed that, as compared to the pure Mg scaffolds, the corrosion rate of the Mg-Zn scaffolds at day 1 was reduced by 81%. Over 28 days of static immersion in r-SBF, the *in vitro* corrosion rate of the Mg-Zn scaffolds decreased from 2.3 ± 0.9 mm/y after 1 day to 0.7 ± 0.1 mm/y after 28 days.
3 The yield strength and elastic modulus of the Mg-Zn scaffolds were 14.5 ± 3.0 and 448.8 ± 42.4 MPa, respectively, which are about 3 times higher than those of the pure Mg scaffolds. During 28 days of *in vitro* biodegradation, the mechanical properties of the Mg-Zn scaffolds remained within the range of those of trabecular bone.
4 The indirect culture of preosteoblasts in the 10% Mg-Zn extracts revealed good cytocompatibility. Although direct cell culture on the Mg-Zn scaffolds showed cytotoxicity, an *in vivo* study needs to be performed to evaluate the biocompatibility of the Mg-Zn scaffolds under real physiological conditions.
5 Preparing coatings on and into the scaffolds or introducing bioactive components inside the scaffold struts to form composites may be explored to further improve the biocompatibility of such 3D printed Mg-Zn scaffolds.

Declaration of Competing Interest

The authors declare that they have no known competing financial interests or personal relationships that could have appeared to influence the work reported in this paper.

Acknowledgements

J.D. thanks the China Scholarship Council (CSC) for financial support. Mr. Ruud Hendrikx at the Department of Materials Science and Engineering, Delft University of Technology, is acknowledged for the XRD analysis. Mr. Michel van den Brink at the Department of Process and Energy, Delft University of Technology, is acknowledged for the ICP-OES analysis. The authors thank Mr. Bart Boshuizen at the Department of Chemical Engineering, Delft University of Technology for his assistance in the XPS measurements. The assistance of Mrs. Agnieszka Kooijman at the Department of Materials Science and Engineering, Delft University of Technology, in electrochemical experiments is also greatly appreciated.

Supplementary materials

Supplementary material associated with this article can be found, in the online version, at doi:10.1016/j.jma.2021.11.018.

References

[1] Y. Li, P. Pavanram, J. Zhou, K. Lietaert, P. Taheri, W. Li, H. San, M.A. L.eeflang, J.M.C. Mol, H. Jahr, A.A. Z.adpoor, Additively manufactured biodegradable porous zinc, Acta Biomater 101 (2020) 609–623.

[2] A.H. Y.usop, A.A. B.akir, N.A. S.haharom, M.R. A.bdul Kadir, H. Hermawan, Porous biodegradable metals for hard tissue scaffolds: a review, Int. J. Biomater. 2012 (2012) 641430.

[3] A. Zadpoor, Current trends in metallic orthopedic biomaterials: from additive manufacturing to bio-functionalization, infection prevention, and beyond, Int. J. Mol. Sci. 19 (2018) 2684.

[4] R. Karunakaran, S. Ortgies, A. Tamayol, F. Bobaru, M.P. S.ealy, Additive manufacturing of magnesium alloys, Bioact. Mater. 5 (2020) 44–54.

[5] J. Jiang, Y.-F. Fu, A short survey of sustainable material extrusion additive manufacturing, Aust. J. Mech. Eng. (2020) 1–10.

[6] A.A. Z.adpoor, Mechanical performance of additively manufactured meta-biomaterials, Acta Biomater 85 (2019) 41–59.

[7] Y. Li, H. Jahr, K. Lietaert, P. Pavanram, A. Yilmaz, L.I. F.ockaert, M.A. L.eeflang, B. Pouran, Y. Gonzalez-Garcia, H. Weinans, J.M.C. Mol, J. Zhou, A.A. Z.adpoor, Additively manufactured biodegradable porous iron, Acta Biomater 77 (2018) 380–393.

[8] X.J. W.ang, S.Q. X.u, S.W. Z.hou, W. Xu, M. Leary, P. Choong, M. Qian, M. Brandt, Y.M. X.ie, Topological design and additive manufacturing of porous metals for bone scaffolds and orthopaedic implants: a review, Biomaterials 83 (2016) 127–141.

[9] J. Ni, H. Ling, S. Zhang, Z. Wang, Z. Peng, C. Benyshek, R. Zan, A.K. M.iri, Z. Li, X. Zhang, J. Lee, K.J. L.ee, H.J. K.im, P. Tebon, T. Hoffman, M.R. D.okmeci, N. Ashammakhi, X. Li, A. Khademhosseini, Three-dimensional printing of metals for biomedical applications, Mater. Today Bio. 3 (2019) 100024.

[10] Y. Li, J. Zhou, P. Pavanram, M.A. L.eeflang, L.I. F.ockaert, B. Pouran, N. Tumer, K.U. S.chroder, J.M.C. Mol, H. Weinans, H. Jahr, A.A. Z.adpoor, Additively manufactured biodegradable porous magnesium, Acta Biomater 67 (2018) 378–392.

[11] A. Kopp, T. Derra, M. Muther, L. Jauer, J.H. S.chleifenbaum, M. Voshage, O. Jung, R. Smeets, N. Kroger, Influence of design and postprocessing parameters on the degradation behavior and mechanical properties of additively manufactured magnesium scaffolds, Acta Biomater 98 (2019) 23–35.

[12] Y. Wang, P. Fu, N. Wang, L. Peng, B. Kang, H. Zeng, G. Yuan, W. Ding, Challenges and solutions for the additive manufacturing of biodegradable magnesium implants, Engineering 6 (2020) 1267–1275.

[13] V. Manakari, G. Parande, M. Gupta, Selective laser melting of magnesium and magnesium alloy powders: a review, Metals 7 (2016) 2.

[14] S. Das, Physical aspects of process control in selective laser sintering of metals, Adv. Eng. Mater. 5 (2003) 701–711.

[15] M. Salehi, S. Maleksaeedi, M.a.B. Sapari, M.L.S. Nai, G.K. M.eenashisundaram, M. Gupta, Additive manufacturing of magnesium–zinc–zirconium (ZK) alloys via capillary-mediated binderless three-dimensional printing, Mater. Des. 169 (2019) 107683.

[16] M. Salehi, S. Maleksaeedi, M.L.S. Nai, M. Gupta, Towards additive manufacturing of magnesium alloys through integration of binderless 3D printing and rapid microwave sintering, Addit. Manuf. 29 (2019) 100790.

[17] edited by T.M.M. Wolff, A. Bals, T. Ebel, R. Willumeit-RöMer, FFF of Mg-Alloys for Biomedical Application, in Magensium Technology 2019, Proceedings of Magensium Technology Symposium at the 148th TMS Annual Meeting, San Antonio, Texas, 2019, in: V.V. Joshi, J.Brian Jordon, D. Orlov, N.R. Neelameggham (Eds.), The Minerals, Metals & Materials Society, Pittsburgh, PA, 2019, pp. 43–49.

[18] J. Dong, Y. Li, P. Lin, M.A. L.eeflang, S. Van Asperen, K. Yu, N. Tumer, B. Norder, A.A. Z.adpoor, J. Zhou, Solvent-cast 3D printing of magnesium scaffolds, Acta Biomater 114 (2020) 497–514.

[19] J. Dong, N. Tümer, N.E. Putra, J. Zhu, Y. Li, M.A. Leeflang, P. Taheri, L.E. Fratila-Apachitei, J.M.C. Mol, A.A. Zadpoor, J. Zhou, Extrusion-based 3D printed magnesium scaffolds with multifunctional MgF2 and MgF2-CaP coatings, Biomater. Sci. (2021).

[20] N.T. K.irkland, J. Lespagnol, N. Birbilis, M.P. S.taiger, A survey of bio–corrosion rates of magnesium alloys, Corros. Sci. 52 (2010) 287–291.

[21] J. Yu, J. Wang, Q. Li, J. Shang, J. Cao, X. Sun, Effect of Zn on microstructures and properties of Mg-Zn alloys prepared by powder metallurgy method, Rare Metal Mat. Eng. 45 (2016) 2757–2762.

[22] S. Cai, T. Lei, N. Li, F. Feng, Effects of Zn on microstructure, mechanical properties and corrosion behavior of Mg–Zn alloys, Mater. Sci. Eng. C. 32 (2012) 2570–2577.

[23] S. Zhang, X. Zhang, C. Zhao, J. Li, Y. Song, C. Xie, H. Tao, Y. Zhang, Y. He, Y. Jiang, Y. Bian, Research on an Mg-Zn alloy as a degradable biomaterial, Acta Biomater 6 (2010) 626–640.

[24] X. Gu, Y. Zheng, Y. Cheng, S. Zhong, T. Xi, *In vitro* corrosion and biocompatibility of binary magnesium alloys, Biomaterials 30 (2009) 484–498.

[25] S. Zhang, J. Li, Y. Song, C. Zhao, X. Zhang, C. Xie, Y. Zhang, H. Tao, Y. He, Y. Jiang, Y. Bian, *In vitro* degradation, hemolysis and MC3T3-E1 cell adhesion of biodegradable Mg–Zn alloy, Mater. Sci. Eng. C-Mater. Biol. Appl. 29 (2009) 1907–1912.

[26] D.B. P.rabhu, P. Gopalakrishnan, K.R. R.avi, Morphological studies on the development of chemical conversion coating on surface of Mg–4 Zn alloy and its corrosion and bio mineralisation behaviour in simulated body fluid, J. Alloys Compd. 812 (2020) 152146.

[27] C.J. B.oehlert, K. Knittel, The microstructure, tensile properties, and creep behavior of Mg–Zn alloys containing 0–4.4 wt.% Zn, Mater. Sci. Eng. A-Struct. Mater. Prop. Microstruct. Process. 417 (2006) 315–321.

[28] H. Tapiero, K.D. T.ew, Trace elements in human physiology and pathology: zinc and metallothioneins, Biomed. Pharmacother. 57 (2003) 399–411.

[29] J. Li, P. Han, W. Ji, Y. Song, S. Zhang, Y. Chen, C. Zhao, F. Zhang, X. Zhang, Y. Jiang, The *in vitro* indirect cytotoxicity test and *in vivo* interface bioactivity evaluation of biodegradable FHA coated Mg–Zn alloys, Mater. Sci. Eng. B-Adv. Funct. Solid-State Mater. 176 (2011) 1785–1788.

[30] W. Yu, D. Chen, Z. Ding, M. Qiu, Z. Zhang, J. Shen, X. Zhang, S. Zhang, Y. He, Z. Shi, Synergistic effect of a biodegradable Mg–Zn alloy on osteogenic activity and anti-biofilm ability: an *in vitro* and *in vivo* study, RSC Adv 6 (2016) 45219–45230.

[31] Z.S. S.eyedraoufi, S. Mirdamadi, Synthesis, microstructure and mechanical properties of porous Mg-Zn scaffolds, J. Mech. Behav. Biomed. Mater. 21 (2013) 1–8.

[32] Y. Yan, Y. Kang, D. Li, K. Yu, T. Xiao, Q. Wang, Y. Deng, H. Fang, D. Jiang, Y. Zhang, Microstructure, mechanical properties and corrosion behavior of porous Mg-6 wt.% Zn scaffolds for bone tissue engineering, J. Mater. Eng. Perform. 27 (2018) 970–984.

[33] A. Oyane, Hyun. Kim, T. Furuya, T. Kokubo, T. Miyazaki, T. Nakamura, Preparation and assessment of revised simulated body fluids, J. Biomed. Mater. Res. Part A. 65A (2003) 188–195.

[34] Y. Xin, T. Hu, P.K. C.hu, *In vitro* studies of biomedical magnesium alloys in a simulated physiological environment: a review, Acta Biomater 7 (2011) 1452–1459.

[35] Biological evaluation of medical devices —Part 12: sample preparation and reference materials, ISO 10993-12:2012 (2012).

[36] J. Fischer, M.H. P.rosenc, M. Wolff, N. Hort, R. Willumeit, F. Feyerabend, Interference of magnesium corrosion with tetrazolium-based cytotoxicity assays, Acta Biomater 6 (2010) 1813–1823.

[37] Y. Zhu, G. Wu, Y.-H. Zhang, Q. Zhao, Growth and characterization of $Mg(OH)_2$ film on magnesium alloy AZ31, Appl. Surf. Sci. 257 (2011) 6129–6137.

[38] Y. Xin, C. Liu, X. Zhang, G. Tang, X. Tian, P.K. C.hu, Corrosion behavior of biomedical AZ91 magnesium alloy in simulated body fluids, J. Mater. Res. 22 (2011) 2004–2011.

[39] M.M. Figueiredo, J.a.F. Gamelas, A.G. M.artins, in: Characterization of Bone and Bone-Based Graft Materials Using FTIR Spectroscopy in Infrared Spectroscopy – Life and Biomedical Sciences, InTechOpen, London, 2012, pp. 315–337. edited by Theophanides Theophile.

[40] F. Khairallah, A. Glisenti, XPS study of MgO nanopowders obtained by different preparation procedures, Surf. Sci. Spectra. 13 (2006) 58–71.

[41] J.E. Q.u, M. Ascencio, L.M. J.iang, S. Omanovic, L.X. Y.ang, Improvement in corrosion resistance of WE43 magnesium alloy by the electrophoretic formation of a ZnO surface coating, J. Coat. Technol. Res. 16 (2019) 1559–1570.

[42] J.E. G.ray-Munro, M. Strong, The mechanism of deposition of calcium phosphate coatings from solution onto magnesium alloy AZ31, J. Biomed. Mater. Res. Part A. 90 (2009) 339–350.

[43] D. Kapinos, B. Augustyn, M. Szymanek, Methods of introducing alloying elements into liquid magnesium, Metall. Foundry Eng. 40 (2014) 141.

[44] J.L. W.ang, F. Witte, T.F. X.i, Y.F. Z.heng, K. Yang, Y.S. Y.ang, D.W. Z.hao, J. Meng, Y.D. L.i, W.R. L.i, K.M. C.han, L. Qin, Recommendation for modifying current cytotoxicity testing standards for biodegradable magnesium-based materials, Acta Biomater 21 (2015) 237–249.

[45] edited by R.M. G.erman, Sintering With a Liquid Phase, in: Randall M. German (Ed.), Sintering: from Empirical Observations to Scientific Principles, Elsevier, 2014, pp. 247–303. edited by.

[46] J.M. S.eok, T. Rajangam, J.E. J.eong, S. Cheong, S.M. J.oo, S.J. O.h, H. Shin, S.H. K.im, S.A. P.ark, Fabrication of 3D plotted scaffold with microporous strands for bone tissue engineering, J. Mat. Chem. B. 8 (2020) 951–960.

[47] Y. Yan, H. Cao, Y. Kang, K. Yu, T. Xiao, J. Luo, Y. Deng, H. Fang, H. Xiong, Y. Dai, Effects of Zn concentration and heat treatment on the microstructure, mechanical properties and corrosion behavior of as-extruded Mg-Zn alloys produced by powder metallurgy, J. Alloys Compd. 693 (2017) 1277–1289.

[48] E. Koç, M.B. K.annan, M. Ünal, E. Candan, Influence of zinc on the microstructure, mechanical properties and *in vitro* corrosion behavior of magnesium–zinc binary alloys, J. Alloys Compd. 648 (2015) 291–296.

[49] G. Song, A. Atrens, Corrosion mechanisms of magnesium alloys, Adv. Eng. Mater. 1 (1999) 11–33.

[50] D. Yin, E. Zhang, S. Zeng, Effect of Zn on mechanical property and corrosion property of extruded Mg-Zn-Mn alloy, Trans. Nonferrous Met. Soc. China. 18 (2008) 763–768.

[51] H.-.Y. Ha, J.-.Y. Kang, J. Yang, C.D. Y.im, B.S. Y.ou, Limitations in the use of the potentiodynamic polarisation curves to investigate the effect of Zn on the corrosion behaviour of as-extruded Mg–Zn binary alloy, Corros. Sci. 75 (2013) 426–433.

[52] H.R. B.akhsheshi-Rad, E. Hamzah, A. Fereidouni-Lotfabadi, M. Daroonparvar, M.a.M. Yajid, M. Mezbahul-Islam, M. Kasiri-Asgarani, M. Medraj, Microstructure and bio-corrosion behavior of Mg-Zn and Mg-Zn-Ca alloys for biomedical applications, Mater. Corros. 65 (2014) 1178–1187.

[53] E. Dayaghi, H.R. B.akhsheshi-Rad, E. Hamzah, A. Akhavan-Farid, A.F. I.smail, M. Aziz, E. Abdolahi, Magnesium-zinc scaffold loaded with tetracycline for tissue engineering application: *in vitro* cell biology and antibacterial activity assessment, Mater. Sci. Eng. C-Mater. Biol. Appl. 102 (2019) 53–65.

[54] H. Yang, B. Jia, Z. Zhang, X. Qu, G. Li, W. Lin, D. Zhu, K. Dai, Y. Zheng, Alloying design of biodegradable zinc as promising bone implants for load-bearing applications, Nat. Commun. 11 (2020) 401.

[55] M.E. M.oussa, H.I. M.ohamed, M.A. W.aly, G.S. A.l-Ganainy, A.B. A.hmed, M.S. T.alaat, Comparison study of Sn and Bi addition on microstructure and bio-degradation rate of as-cast Mg-4wt% Zn alloy without and with Ca-P coating, J. Alloys Compd. 792 (2019) 1239–1247.

[56] W. Jiang, J. Wang, W. Zhao, Q. Liu, D. Jiang, S. Guo, Effect of Sn addition on the mechanical properties and bio-corrosion behavior of cytocompatible Mg–4 Zn based alloys, J. Magnes. Alloy. 7 (2019) 15–26.

[57] M. Sabbaghian, R. Mahmudi, K.S. S.hin, Microstructure, texture, mechanical properties and biodegradability of extruded Mg–4Zn–xMn alloys, Mater. Sci. Eng. A-Struct. Mater. Prop. Microstruct. Process. 792 (2020) 139828.

[58] C. Gao, M. Yao, S. Li, P. Feng, S. Peng, C. Shuai, Highly biodegradable and bioactive Fe-Pd-bredigite biocomposites prepared by selective laser melting, J. Adv. Res. 20 (2019) 91–104.

[59] Y. Song, E.-.H. Han, D. Shan, C.D. Y.im, B.S. Y.ou, The effect of Zn concentration on the corrosion behavior of Mg–xZn alloys, Corros. Sci. 65 (2012) 322–330.

[60] S.M. A.hmadi, S.A. Y.avari, R. Wauthle, B. Pouran, J. Schrooten, H. Weinans, A.A. Z.adpoor, Additively manufactured open-cell porous biomaterials made from six different space-filling unit cells: the mechanical and morphological properties, Materials (Basel) 8 (2015) 1871–1896.

[61] F.S.L. Bobbert, K. Lietaert, A.A. E.ftekhari, B. Pouran, S.M. A.hmadi, H. Weinans, A.A. Z.adpoor, Additively manufactured metallic porous biomaterials based on minimal surfaces: a unique combination of topological, mechanical, and mass transport properties, Acta Biomater 53 (2017) 572–584.

[62] Yu.N. Podrezov, L.G. S.htyka, A.D.G. Verbylo, Strain-hardening of porous iron under uniaxial compression, Powder Metall. Met. Ceram. 39 (2000) 92–96.

[63] M. Hradilová, D. Vojtěch, J. Kubásek, J. Čapek, M. Vlach, Structural and mechanical characteristics of Mg–4Zn and Mg–4Zn–0.4Ca alloys after different thermal and mechanical processing routes, Mater. Sci. Eng. A-Struct. Mater. Prop. Microstruct. Process. 586 (2013) 284–291.

[64] D. Zhao, F. Witte, F. Lu, J. Wang, J. Li, L. Qin, Current status on clinical applications of magnesium-based orthopaedic implants: a review from clinical translational perspective, Biomaterials 112 (2017) 287–302.

[65] M. Yazdimamaghani, M. Razavi, D. Vashaee, K. Moharamzadeh, A.R. B.occaccini, L. Tayebi, Porous magnesium-based scaffolds for tissue engineering, Mater. Sci. Eng. C-Mater. Biol. Appl. 71 (2017) 1253–1266.

[66] R. Hedayati, S.M. A.hmadi, K. Lietaert, N. Tumer, Y. Li, S. Amin Yavari, A.A. Z.adpoor, Fatigue and quasi-static mechanical behavior of bio-degradable porous biomaterials based on magnesium alloys, J. Biomed. Mater. Res. Part A. 106 (2018) 1798–1811.

[67] Biological evaluation of medical devices—Part 5: tests for *in vitro* cytotoxicity, ISO 10993-5:2009 (2009).

[68] Y. Zhang, J. Xu, Y.C. R.uan, M.K. Y.u, M. O'laughlin, H. Wise, D. Chen, L. Tian, D. Shi, J. Wang, S. Chen, J.Q. F.eng, D.H. C.how, X. Xie, L. Zheng, L. Huang, S. Huang, K. Leung, N. Lu, L. Zhao, H. Li, D. Zhao, X. Guo, K. Chan, F. Witte, H.C. C.han, Y. Zheng, L. Qin, Implant-derived magnesium induces local neuronal production of CGRP to improve bone-fracture healing in rats, Nat. Med. 22 (2016) 1160–1169.

[69] A. Yamamoto, R. Honma, M. Sumita, Cytotoxicity evaluation of 43 metal salts using murine fibroblasts and osteoblastic cells, J. Biomed. Mater. Res. 39 (1998) 331–340.

[70] Atsuo Ito, Haruo Kawamura, Makoto Otsuka, Masako Ikeuchi, Hajime Ohgushi, Kunio Ishikawa, Kazuo Onuma, Noriko Kanzaki, Yu Sogo, N. Ichinose, Zinc-releasing calcium phosphate for stimulating bone formation, Mater. Sci. Eng. C-Mater. Biol. Appl. 22 (2002) 21–25.

[71] G. Jin, H. Cao, Y. Qiao, F. Meng, H. Zhu, X. Liu, Osteogenic activity and antibacterial effect of zinc ion implanted titanium, Colloids Surf. B: Biointerfaces. 117 (2014) 158–165.

[72] D. Chen, Y. He, H. Tao, Y. Zhang, Y. Jiang, X. Zhang, S. Zhang, Biocompatibility of magnesium-zinc alloy in biodegradable orthopedic implants, Int. J. Mol. Med. 28 (2011) 343–348.

[73] Y. He, H. Tao, Y. Zhang, Y. Jiang, S. Zhang, C. Zhao, J. Li, B. Zhang, Y. Song, X. Zhang, Biocompatibility of bio-Mg-Zn alloy within bone with heart, liver, kidney and spleen, Sci. Bull. 54 (2009) 484–491.